Modelling framework for asynchronous land-atmosphere coupling using NASA GISS ModelE and LPJ-LMfire: Design, Application and Evaluation for the 2.5ka period

Ram Singh[1,2], Alexander Koch[4], Allegra N LeGrande[2,1], Kostas Tsigaridis[1,2], Riovie D Ramos[5], Francis Ludlow[6], Igor Aleinov[1,2], Reto Ruedy[2,3], Jed O Kaplan[7]

[1] Center for Climate Systems Research, Columbia University, New York, USA
[2] NASA Goddard Institute for Space Studies, New York, NY-10025, USA
[3] SciSpace LLC, New York, NY, USA
[4] Department of Earth Sciences, The University of Hong Kong, Hong Kong SAR, China
[5] Earth Observatory of Singapore, Singapore
[6] Department of History, and Trinity Centre for Environmental Humanities, School of Histories and Humanities, Trinity College, Dublin 2, Ireland
[7] Department of Earth, Energy, and Environment, University of Calgary, Calgary AB, Canada

Correspondence to: Ram Singh (ram.bhari85@gmail.com)

Abstract

While paleoclimate simulations have been a priority for Earth system modelers over the past three decades, little attention has been paid to the period between the mid-Holocene (6ka) and the Last Millennium, although this is an important period for the emergence of complex societies. Here, we consider the climate of 2500 BP (before present or 550 BCE), a period when compared to late preindustrial time, greenhouse gas concentrations were slightly lower, and orbital forcing led to a stronger seasonal cycle in high latitude insolation. To capture the influence of land cover on climate, we asynchronously coupled the NASA GISS ModelE Earth system model with the LPJ-LMfire dynamic global vegetation model. We simulated global climate and assessed our results in the context of independent paleoclimate reconstructions. We also explored a set of combinations of model performance parameters (bias and variability) and demonstrated their importance for the asynchronous coupling framework. The asynchronously coupled model system shows strong vegetation-albedo feedback on climate and is comparatively more sensitive to the bias correction than the internal model variability and green Sahara conditions. In the absence of a bias correction, while driving LPJ-LMfire in the coupling process, ModelE drifts towards colder conditions in the high latitudes of the Northern Hemisphere in response to land cover simulated by LPJ-LMfire. A regional precipitation response is also prominent in the various combinations of the coupled model system, with a substantial intensification of the Summer Indian Monsoon and a drying pattern over Europe. Evaluation of the simulated climate against reconstructions of temperature from multiple proxies and the isotopic composition of precipitation ($\delta^{18}O_p$) from speleothems demonstrated the skill of ModelE in simulating past climate. A regional analysis of the simulated vegetation-climate response further confirmed the validity of this approach. The NASA GISS ModelE was found to be particularly sensitive to the representation of shrubs and this land cover type requires particular attention as a potentially important driver of climate in regions where shrubs are abundant. Our results further demonstrate the importance of bias correction in coupled paleoclimate simulations. This study presents a generalized framework for incorporating biogeophysical responses into climate models without dynamic vegetation, for simulating past climates, in line with the recommendations of the Paleoclimate Modelling Intercomparison Project (PMIP).

1. Introduction

Earth system models (ESMs) are widely applied in paleoclimate experiments as an "out of sample" exercise to evaluate the overall quality of the model, and to better understand climate system responses to external forcings. In many paleoclimate modeling studies, it has been demonstrated that the inclusion of biogeophysical and biogeochemical feedbacks between land and atmosphere are essential to simulate the magnitude and spatial pattern of climate change that is consistent with independent reconstructions (Betts, 2000; Claussen, 1997; Cox et al., 2000; Doherty et al., 2000; Strandberg et al., 2014a). The importance of land-atmosphere feedbacks for past climate has been shown to be particularly high in the context of the mid-Holocene and last glacial inception periods (Braconnot et al., 2012; Collins et al., 2017; Harrison et al., 2015; Jahn et al., 2005; Kubatzki and Claussen, 1998; Sha et al., 2019; Shanahan et al., 2015; Tierney et al., 2017). For example, for the African Humid Period of the mid-Holocene, numerous studies have demonstrated that greenhouse gases (CO_2, N_2O, CH_4) and orbital forcing are alone insufficient for models to simulate climate that is consistent with independent paleoclimate reconstructions. The inclusion of land-atmosphere feedbacks via interactive dynamic vegetation modeling or prescribed vegetation distributions helps to reduce model-proxy discrepancies (Chandan and Peltier, 2020; Charney, 1975; Dallmeyer et al., 2021; Pausata et al., 2016; Rachmayani et al., 2015; Singh et al., 2023; Thompson et al., 2021; Tiwari et al., 2023; Velasquez et al., 2021). For this reason, more recent protocols (PMIP4; Otto-Bliesner et al., 2017) for simulations of the mid-Holocene specify that the land cover boundary condition should include shrub vegetation in northern Africa with greater extent than the present (the so-called "Green Sahara"), as well as an expansion of trees and shrubs at high northern latitudes.

Instead of prescribing land cover boundary conditions in an earth system model, it may be desirable to employ a coupled model where that allows interaction between climate and vegetation. While several modern earth system models include a dynamic representation of land cover, in climate models (regional and global) that lack a coupled dynamic vegetation component a well-established technique to capture land-atmosphere feedbacks is to use asynchronous coupling. In this type of coupling, climate model output is used to drive an offline vegetation model that then returns a land cover boundary condition to the climate model.

To quantify the feedback between land and atmosphere and improve the fidelity of the paleoclimate simulation, asynchronous coupling typically involves running a climate model simulation for a period of a few decades, after which the mean climate state is passed to a vegetation model that in-turn produces a land cover boundary condition for the climate model. This process is repeated until climate reaches equilibrium, defined as insignificant changes in key outputs, e.g., 2m temperature, from one cycle to the next.

Texier et al., (1997) used an iterative asynchronous coupling between the LMD Atmospheric General Circulation Model (AGCM) and the BIOME1 vegetation model to produce an improved climate for the mid-Holocene (6ka) period and found that inclusion of land-atmosphere feedbacks led to simulations of temperatures at high latitudes and precipitation over West Africa that were more consistent with independent paleoclimate reconstructions compared to atmosphere-only simulations. de Noblet et al., (1996) used a similar coupling to highlight the role of biogeophysical feedback in glacial initiation around 115ka ago. Asynchronous coupling has also been used with regional climate models (RCMs). Kjellstroem et al., (2009) and Velasquez et al. (2021) both used asynchronous coupling between an RCM and land cover model to simulate the climate of Europe at the Last Glacial Maximum. Both studies demonstrated the importance of land cover in improving agreement with reconstructions and paleoenvironmental proxies.

This study has two objectives. First, we present a generalized design for asynchronously coupling the NASA GISS ModelE2.1 climate model (Kelley et al., 2020) with the LPJ-LMfire DGVM (Pfeiffer et al., 2013) to simulate climate and include biogeophysical land-atmosphere feedbacks. Second, we demonstrate the utility of this asynchronous coupling framework for a paleoclimatic period that has not been the traditional focus of paleoclimate modeling (2.5ka) and evaluate the model results against independent paleoclimate reconstructions for that period.

2.5ka represents a time that is nearest to the present day among the different periods selected under the coordinated effort of the Paleoclimate Model Intercomparison Project (PMIP4). It is interesting because it represents an important period for the emergence of complex societies across Eurasia (Iron Age, Classical Antiquity, early Imperial China) and elsewhere. During this

era, favorable climate conditions around the Mediterranean might have influenced the emergence of the golden age of Greece, the Roman classical period, and other empires of Southern Europe, North Africa, and southwest Asia (Lamb, 1982; Reale and Dirmeyer, 2000). On the other hand, adverse climate conditions due to volcanic eruptions and a series of arid phases during this period may have had a negative impact on Egyptian civilization around the Nile and Mesopotamian civilization around the Euphrates and Tigris rivers. 2.5ka is thus a key period for the study of human-environment interactions and the history of climate and society, where we may assess societal vulnerability to climate variability on different scales (Ludlow and Manning, 2021; Manning et al., 2017; Mikhail, 2015; Petit-Maire and Guo, 1998; Singh et al., 2023).

Section 2 describes the models used in this study (Section 2.1), the initial control run for 2.5ka, and a stepwise description of the asynchronous coupling framework, including variable exchange and processing (Sections 2.2 and 2.3). Section 3 presents the experimental design for implementing the asynchronous coupled system and evaluates the PFT mapping schemes. In Section 4, we evaluate the simulated 2.5ka climate using the ModelE–LPJ asynchronous coupling framework against multi-proxy temperature reconstructions (Kaufman et al., 2020) and additionally utilized the model's capabilities to simulate the isotopic composition of water in precipitation (δ^{18}Op) to compare with the Speleothem Isotope Synthesis and Analysis (SISAL) version 2 database (Comas-Bru et al., 2020). Section 5 provides the analysis and comparison of model-simulated climate under various experimental configurations.

2. Models and asynchronous coupling framework

2.1.1 NASA GISS ModelE2.1: NASA GISS ModelE2.1 (Kelley et al., 2020) is the climate model of the NASA Goddard Institute for Space Studies (GISS) currently used in Climate Model Intercomparison Project (CMIP) phase 6 (Eyring et al., 2016). We used the NINT (Non-Interactive; physics version 1 in CMIP6) GISS ModelE2.1 version where aerosols and ozone are precomputed from the prognostic, but much more computationally demanding, chemistry and aerosols version of the model OMA (One Moment Aerosols; physics version 3 in CMIP6; (Bauer et al., 2020)). In our simulations, the GISS ModelE2.1 atmosphere has a horizontal resolution of 2°x2.5° (latitude/longitude) with 40 vertical layers, and the top of the atmosphere at 0.1 hPa. The ModelE2.1 atmosphere has a smooth transition from sigma layers to constant pressure layers

centered at 100hPa. The atmosphere is coupled to the GISS Ocean v1 model, which runs at a resolution of 1°x1.25° (latitude/longitude) with 40 depth layers to the ocean bottom. While the biogeophysical properties of land cover are simulated with the Ent Terrestrial Biosphere Model (Ent TBM; Kiang 2012; Kim et al., 2015)), as part of ModelE2.1 (Ito et al., 2020), Ent relies on a prescribed vegetation map and as such does not simulate changes in land cover over time. To capture the influence of climate change on land cover and biogeophysical feedbacks between land and atmosphere, asynchronous coupling with LPJ-LMfire (or any other DGVM) is currently required.

2.1.2 LPJ-LMfire: We used the LPJ-LMfire DGVM (v1.4.0) to simulate the land cover boundary conditions in our experiments. LPJ-LMfire (Kaplan et al., 2022; Pfeiffer et al., 2013) is an evolution of LPJ (Sitch et al., 2003) and is a process-based, large-scale representation of plant growth and decay, vegetation demographics and ecological disturbance, and water and carbon exchanges between the land and the atmosphere. LPJ-LMfire has been successfully validated for simulating present-day biogeography and fire regime characteristics, and its outputs have been compared against contemporary observations (Pfeiffer et al., 2013; Sitch et al., 2003; Thonicke et al., 2010). For this study, we simulated land cover boundary conditions at a horizontal resolution of 0.5°x0.5°. LPJ-LMfire is driven by monthly climate fields (temperature, precipitation, cloud cover, wind, and lightning), static maps of topography and soil texture, and an annual global value of atmospheric CO_2 concentration. LPJ-LMfire simulates land cover in the form of fractional coverages of nine plant functional types (PFTs), including tropical, temperate, and boreal trees, and tropical and extratropical herbaceous vegetation (Table 1). CO_2, soil texture and topography data used to drive LPJ-LMfire are described in Pfeiffer et al. (2013, Table 3). For 2.5ka simulations, we set atmospheric CO_2 concentrations to 271.4 ppm (Kaplan et al., 2012). The sum of PFT fractional cover per grid box does not need to equal unity; when it is less than one the remainder is considered bare ground.

Table 1: - Summary of climate and land cover variables exchanged between NASA GISS ModelE and LPJ-LMfire model for asynchronous coupling process. Column 1 and 2 shows the output and input climate variables from GISS ModelE to LPJ-LMfire models, whereas the columns 3 and 4 lists the output and input plant functional types (PFTs) from LPJ-LMfire to GISS ModelE.

173

GISS Output	**LPJ -LMfire Input**	**Annual cycle climatology and variability (standard deviation) over the period of interest (100 Years)**	**LPJ-LMfire Output Vegetation (PFTs)**	**LPJ-LMfire to GISS ModelE (Ent) Vegetation Mapping (Vegetation cover type, Leaf area index and vegetation heights)**	**GISS ModelE (Ent) Vegetation (PFTs)**
Surface Air Temperature (°C)	Surface Air Temperature (°C)		Tropical Broadleaf Evergreen		Evergreen Broadleaf Late Succession
Precipitation (mm/day)	Precipitation (mm/day)		Tropical Broadleaf Raingreen		Evergreen Needleleaf Late Succession
	Number of wet days				
Diurnal Surf. Air Temp Range (°C)	Diurnal Surf. Air Temp Range (°C)		Temperate Needleleaf Evergreen		Cold Deciduous Broadleaf Late Succession
Surface Wind Speed (m/sec)	Surface Wind Speed (m/sec)		Temperate Broadleaf Evergreen		Drought Deciduous Broadleaf
Moist Convective Air Mass Flux ($kg/m^2/sec$)	Lightning Density ($strokes/Km^2/day$)		Temperate Broadleaf Summergreen		Deciduous Needleleaf
			Boreal Needleleaf Evergreen		Cold Adapted Shrub
			Boreal Summergreen		Arid Adapted Shrub
			C3 Perennial Grass		C3 Grass Perennial
			C4 Perennial Grass		C4 Grass
					C3 Grass Annual
					Arctic C3 Grass
					Bright Bare Soil
					Dark Bare Soil

174

2.2. 2.5ka Simulation setup (Initial control run using ModelE)

We started the 2.5ka and preindustrial (PI) control experiments following the PMIP4 and CMIP6 protocols (Eyring et al., 2016; Kageyama et al., 2018). The PI simulation uses preindustrial (year 1850) GHG concentrations and a modern continental configuration and serves as the reference experiment for designing the boundary conditions for past time slices studied in PMIP4. GHG and orbital forcings for the preindustrial (PI) control experiment correspond to levels observed in 1850 CE (CO_2: 284 ppm, N_2O: 273 ppb, CH_4: 808 ppb). For the 2.5ka control experiment, orbital parameters (Berger et al., 2006) were specified for 2,500 years BP (before present ~550 BCE), and greenhouse gas CO_2, N_2O, and CH_4 were set to ~279 ppm, ~266 ppb, and 610 ppb, respectively (Köhler et al., 2017; Loulergue et al., 2008; Otto-Bliesner et al., 2017; Schneider et al., 2013; Siegenthaler et al., 2005). We considered only natural emissions as sources of aerosols in the atmosphere, zeroing-out any anthropogenic contribution to aerosol and aerosol precursors. For biomass burning, in the absence of any better estimate, we assumed that the emissions provided by CEDS (Hoesly et al., 2018) for the year 1750 are all natural. Land cover consists of the fractional coverages of 13 plant functional types (PFTs) and includes vegetation height and leaf area index (LAI). For the PI and initial (0^{th} order) simulations, land cover type and monthly-varying LAI were derived from satellite (MODIS) data (Gao et al., 2008; Kattge et al., 2011; Myneni et al., 2002; Tian et al., 2002a, b; Yang et al., 2006) and vegetation height from Simard et al., (2011). We also used the mid-Holocene (6k) vegetation under the PMIP4 protocol, which is linearly interpolated to 2.5ka period and details of vegetation cover changes (Singh et al., 2023; Figure S2) and associated impacts on the northern hemisphere climate due to the inclusion of scaled PMIP4 vegetation using the interactive chemistry version of NASA GISS ModelE2.1 (MATRIX) are discussed in (Singh et al., 2023).

2.3 Asynchronous coupling framework

The asynchronous coupling between ModelE and LPJ-LMfire is summarized in Figure 1. For each iteration, ModelE simulated climate is used by LPJ-LMfire which returns the PFT fractional cover, LAI, and vegetation height that are used as boundary conditions for the next ModelE simulation.

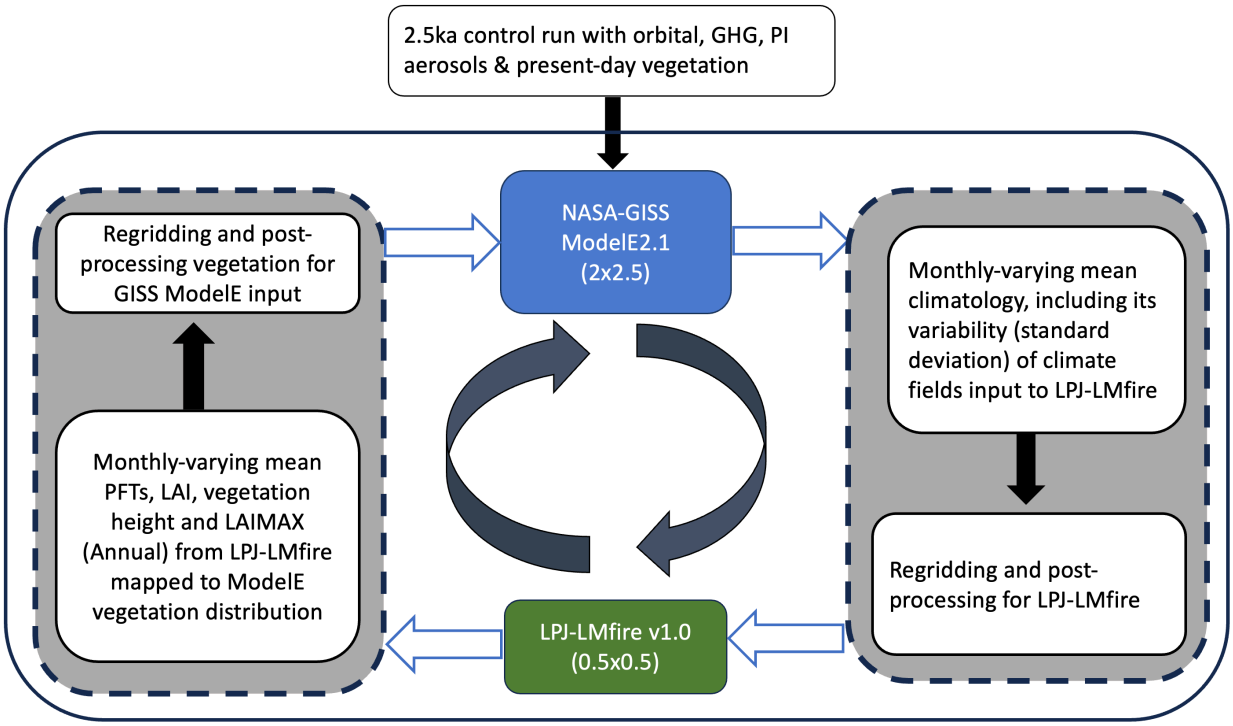

Figure 1: Flow diagram for the asynchronous coupling framework between GISS ModelE2.1 and LPJ-LMfire models. For the climate fields input to LPJ-LMfire refer to (Table 1, Column 1) and LPJ-LMfire PFTs (Table 1, Column 3)

2.3.1 GISS ModelE2.1 simulations: Climatological monthly mean climate (Table 1, Column 1) for a 100-year period was extracted from a well equilibrated ModelE simulation. To assess interannual variability with monthly resolution, we calculated the standard deviation of the decadal mean data for each month across the 100-year equilibrium period.

2.3.2. LPJ-LMfire simulations: All climate variables except diurnal temperature range, wet days, and lightning density were provided directly from the ModelE output. For derived climate variables, the additional processing steps are described below.

Diurnal temperature range was calculated as the difference of the monthly-mean daily maximum and minimum temperatures as simulated by ModelE. Wet days were calculated from modelled precipitation based on an empirical relationship between present-day monthly total precipitation and the number of wet days per month. To quantify this relationship, we performed a nonlinear regression between monthly total precipitation and the number of days with measurable

precipitation using the CRU TS 4.0 gridded climate fields (Harris et al., 2020). Using those data, we developed a set of regression coefficients for every land gridcell that allowed us to estimate wet days for any paleoclimate period based only on monthly total precipitation. Lightning density was estimated based on modelled convective mass flux following Magi (2015). However, the feedback to climate due to fire-driven emissions are not included, as accounting for them would require active atmospheric chemistry and transport, which are not included in LPJ-LMfire.

Because LPJ-LMfire requires a timeseries of interannually varying climate forcing to run, we processed the climatological monthly mean climate produced by the ModelE for use with the vegetation model. In brief, ModelE climate was converted into anomalies by differencing the paleoclimate simulation with ModelE simulated climate for the late 20th century (1951-2000). The resulting climate anomalies were bilinearly interpolated to a 0.5°x0.5° grid and added to a baseline climate based on observations over 1951-2000. The resulting climatology was expanded to a 1020-year-long time series by adding interannual variability in the form of detrended and randomized climate anomalies from the 20th Century Reanalysis (Compo et al., 2011). LPJ requires climate input data with interannual variability because fires and other disturbance events occur only in years with anomalous climate, for example, hot or dry years Sitch et al. (2003). Driving the model with climatological mean climate will result in disturbance frequencies that are lower than the expected mean that in some regions would lead to an overabundance of tree cover when we would expect herbaceous vegetation. For further details on this process, see (Hamilton et al., 2018). Because LPJ-LMfire is computationally inexpensive, we ran each simulation for 1020 years. While the composition and characteristics of aboveground vegetation comes into equilibrium with climate after a few centuries of simulation, a millennium-long simulation brings the terrestrial carbon pools into equilibrium as well. The land cover boundary conditions returned to the climate model represent the mean modeled vegetation cover over the final 250 years of the LPJ-LMfire simulation.

2.3.3. LPJ-LMfire to GISS ModelE vegetation mapping: LPJ-LMfire simulates land cover in the form of nine PFTs, while in GISS ModelE the vegetation component (Ent TBM) recognizes 13 PFTs. We mapped the LPJ-LMfire generated PFT cover, LAI, LAIMAX, and vegetation height

to the GISS ModelE2.1 (Ent) PFTs in order to feed it to the ModelE (Table 1, Column 3 & 4). The main points for the LPJ-LMfire to GISS vegetation mapping are the following:

- Early and late-successional PFTs were approximated from the LPJ-LMfire output using the model simulated fire frequency and monthly burned area fraction. High fire frequency favors early-successional PFTs because the time between disturbances is shorter than that required for establishment. By definition, late-successional PFTs require extended periods of low disturbance to persist within the ecosystem. However, because successional state is indistinguishable in the satellite-driven reference vegetation for the historical period used as the boundary condition for ModelE, we combined early and late successional PFTs in our simulations.
- LPJ-LMfire does not have a specific PFT for shrubs (arid and cold), while Ent does. To estimate shrub cover in LPJ-LMfire, we used LPJ-LMfire simulated tree height for the tropical broadleaf raingreen, temperate broadleaf summergreen, and boreal summergreen PFTs and specified that trees with height lower than a globally-uniform predefined threshold were considered to be shrubs (Table TS1).
- Ent has an Arctic grass PFT while LPJ-LMfire does not. To estimate Arctic grass cover we used the C_3 grass PFT in LPJ-LMfire and specified it as Arctic grass in regions where the boreal summergreen PFT was also present. LPJ-LMfire also does not distinguish between annual and perennial grasses, and so to map these to Ent we assumed that these were present in equal fractions among the simulated C_3 grass in the LPJ-LMfire simulation.
- The non-vegetated fraction of a grid cell is assigned to the bare soil, and the distribution of bright and dark soil color heterogeneity is classified/redistributed based on the present-day structure of soils over a grid cell.

Of particular importance to our coupled model simulations was that the PFTs simulated by LPJ-LMfire do not explicitly include a shrub type. To approximately distinguish tree from shrub cover, we generated three LPJ-to-GISS mapping schemes that differed on how shrubs are specified. A set of possible changes in various PFT classifications are adopted based on the comparison with GISS vegetation distribution and the categorized mapping methodologies. These mappings, summarized in table TS1, differ in the height threshold of trees to be re-categorized as cold and

arid shrubs, and the fraction of perennial grass re-categorized into perennial and arctic grasses. Also, the monthly leaf area index (LAI) and vegetation height is readjusted using the weighted mean for remapped LPJ-LMfire vegetation PFTs.

2.3.4. Step 4. Post-processing of vegetation files: LPJ-LMfire model generates output at a horizontal resolution of 0.5°x0.5°. We resampled the output vegetation information to the 2.0°x2.5° grid used by ModelE2.1. In a few cases, land cover extrapolated using a nearest-neighbor approach was to cover all the grid cells identified as land in the ModelE standard land-sea mask.

3 Experimental Design

Apart from evaluating the framework for the PI control period, we designed a set of experiments to evaluate various aspects of the simulated climate, including model bias, and variability in both the climate and vegetation models. For example, one known limitation in the current version of ModelE is a wintertime cold bias over the Arctic in simulations covering the historical period (Kelley et al., 2020).

Table 2 shows the combinations of the model metrics selected to explore the utility of the asynchronous coupling framework and their impact on simulated climate. Run names are designated using Time (1850, 2.5k), Vegetation source (PI, GS), Bias Correction (BC) and Interannual Variability (LPJ, GISS) separated by "_". For example, '1850_PI_ctrl' and '2.5k_PI_ctrl' denote the 1000-year-long PI and 2.5k runs with GISS PI vegetation. GS stands for Green Sahara and PI = Pre-Industrial. An "x" denotes the absence of a particular criterion (default state). Run '1850_PI_ctrl' (row 1 in table 2) was performed to evaluate the vegetation mapping scheme and to select the appropriate scheme for asynchronous coupling, whereas '2.5k_PI_ctrl' (row 2 in table 2) was used as the 0^{th} order control run for 2.5ka period with present-day vegetation distribution. Runs '2.5k_PI_BC_LPJ', '2.5k_PI_x_x', and '2.5k_PI_x_GISS' are three branches extended from '2.5k_PI_ctrl' with the combinations of bias correction and interannual variability from LPJ and GISS models. For the '2.5k_GS_x_GISS' and '2.5k_GS_BC_GISS' simulations, we initialized the land cover boundary conditions to approximate 2.5ka by linearly interpolating cover fractions between the 6ka land cover prescribed under the PMIP4 protocol (Otto-Bliesner et al., 2017) and the PI reference dataset and extended the 0^{th} order 2.ka control ('2.5k_PI_ctrl')

316 before branching out the experiments ‘2.5k_GS_x_GISS’ and ‘2.5k_GS_BC_GISS’. Details of
317 the 6ka land cover boundary conditions for PMIP4 and associated impacts on Northern
318 Hemisphere climate using the interactive chemistry version of NASA GISS ModelE2.1
319 (MATRIX) are discussed by (Singh et al., 2023). Model equilibrium is determined using the
320 threshold that the absolute value of the decadal-mean planetary radiative imbalance must be < 0.2
321 W m^{-2}, along with the surface temperature trend (absolute value <0.1 °C/50 years). Convergence
322 across iterations is evaluated by comparing the annual mean climate state and vegetation
323 distributions between successive iterations.

Table 2: - Summary of experiments performed to explore and evaluate the GISS ModelE - LPJ-LMFire model asynchronous coupling framework. See text for explanation of the run naming convention.

Run Name	Initial Vegetation Cover	Bias correction	Interannual Variability	Number of Iterations/total number of years	Remark
1850_PI_ctrl	Used to evaluate the LPJ to GISS vegetation mapping schemes GHG Forcing: CO_2: 284 ppm, N_2O: 273 ppb, CH_4: 808 ppb				
2.5k_PI_ctrl	1000-year-long control; base run to branch out the other simulations GHG Forcing: CO_2: 279 ppm, N_2O: 266 ppb, and CH_4: 610 ppb				
2.5k_PI_BC_LPJ	GISS PI vegetation	YES	LPJ	5/750 years	converged
2.5k_PI_x_x	GISS PI vegetation	No	No	2/270 years	Too cold in 3rd iteration diverging
2.5k_PI_x_GISS	GISS PI vegetation	No	GISS ModelE (100years)	4/550 years	Too cold diverging
2.5k_GS_x_GISS	GISS PI vegetation + Green Sahara+ Boreal Forest	No	GISS ModelE (100years)	5/1150 years	Too cold diverging
2.5k_GS_BC_GISS	GISS PI vegetation + Green Sahara+ Boreal Forest	YES	GISS ModelE (100years)	4/1000 years	converged

* Convergence means the final model simulation has a similar climatology with the previous iteration, whereas divergence means the model is drifting away from the expected states.

3.1 Evaluation & Validation of LPJ-GISS Mapping Methodologies

We used the standard present-day land cover boundary conditions described for ModelE2.1 (Kelley et al., 2020) for the initial 0^{th}-order iteration of the pre-industrial and 2.5ka control climate simulations. This land cover dataset is based on satellite observations (Gao et al., 2008; Myneni et al., 2002; Tian et al., 2002a, 2002b; Yang et al., 2006) from the Moderate Resolution Imaging Spectroradiometer (MODIS), with leaf area index (LAI) from the TRY database (Kattge et al., 2011), and vegetation height (Simard et al., 2011) from the Geoscience Laser Altimeter System (GLAS). Branches of the 2.5ka run for green Sahara conditions are started using the linearly interpolated vegetations for 2.5ka from the 6ka vegetation distribution defined based on the PMIP4 protocol (Otto-Bliesner et al., 2017; Singh et al., 2023). These land cover boundary conditions are shown as the fractional coverage of 13 PFTs (including bare soils) (Supplementary Figs. S1 and S2). In these figures, bare dark and bare bright are merged into a single bare soil fractional cover.

The ModelE2.1 pre-industrial (PI) control run initialized with the present-day land cover boundary condition is processed through the asynchronous coupling framework to evaluate the mapping scheme for converting LPJ PFTs to GISS (Ent) PFTs. We tested three sets of LPJ-to-GISS mapping schemes as required in the asynchronous coupling framework. Differences among the mapping schemes are described in supplementary table TS1. Three parallel control runs are performed for 100 years, each initialized with the vegetation distribution that corresponds to the corresponding mapping scheme and compared to the mean climate state of the parent PI control run.

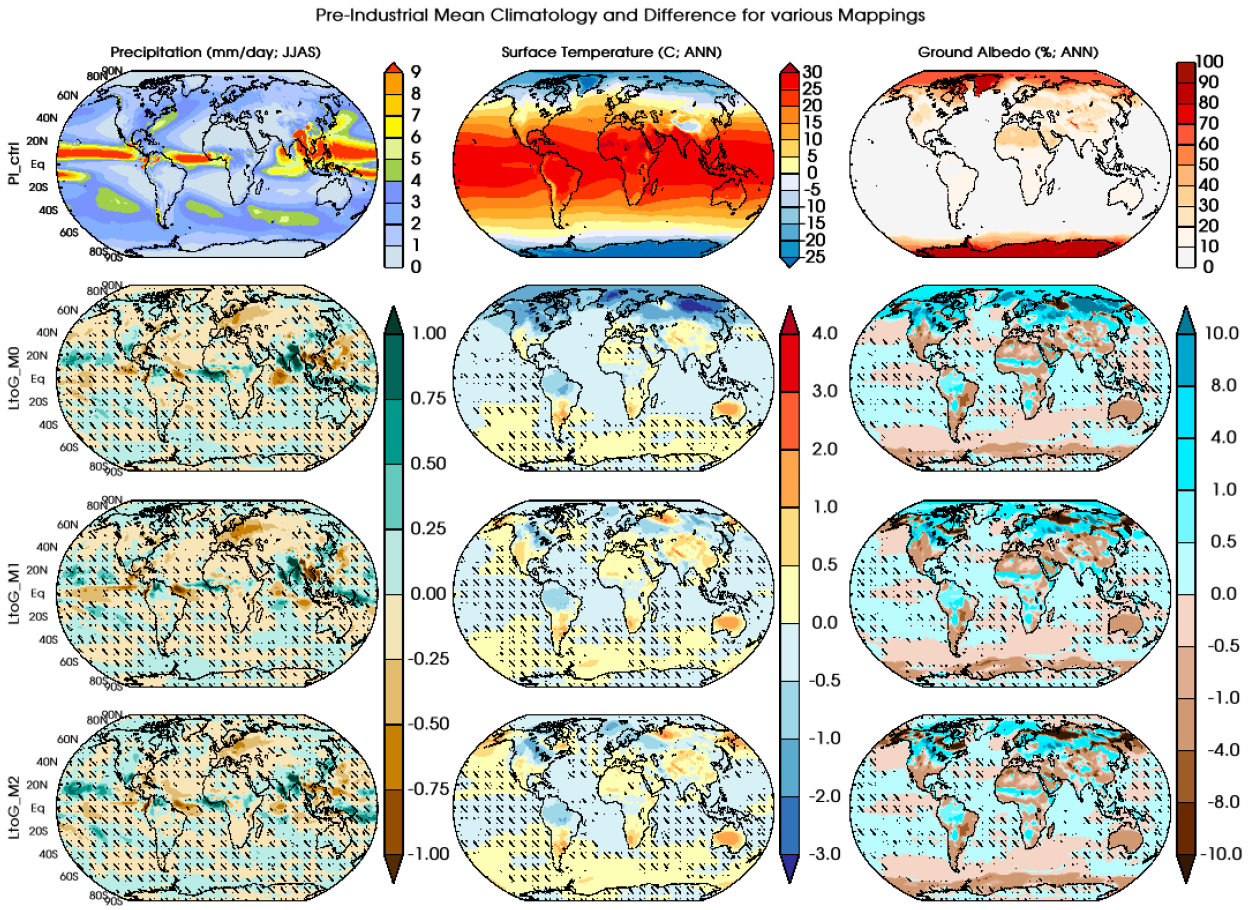

354

355 **Figure 2.** Comparison of seasonal climate metrics between the PI control and different vegetation
356 mapping. Top row shows the mean climatology for precipitation (mm/day; JJAS), surface air
357 temperature (°C; ANN) and ground albedo (%; ANN) and rows 2 to 4 shows the differences in
358 mean climate for the mappings LtoG_M0, LtoG_M1 and LtoG_M2, respectively. Stippling
359 indicates the region over which change is not statistically significant at a 95% confidence interval
360 (Used the student's t-test).

361

362 The mapping schemes LtoG_M1 and LtoG_M2 (supplementary table TS1) generate a similar
363 spatial structure of annual surface air temperature with broadly similar regional characteristics
364 (Fig. 2). A shift towards colder climates of 2-3 °C in mean annual temperature over the higher
365 latitudes of the Northern hemisphere is simulated when using the mapping scheme LtoG_M0,
366 which is not present when using the other mapping schemes (LtoG_M1 and LtoG_M2). We
367 selected forests into shrubs to match the missing PFTs in ModelE vegetation distributions based
368 upon the tree height (Table TS1). In these mapping schemes, the fraction of boreal tree PFTs

assigned to cold shrubs depends on simulated tree height, which is, in turn, influenced by surface temperature (Bonan, 2008; Bonan et al., 1992; Li et al., 2013; Thomas and Rowntree, 1992). In the mapping LtoG_M0, the fractional cover of boreal tree PFTs was reduced significantly, leading to an increase in ground albedo (up to 10%), which led to the model drifting towards comparatively colder climate conditions. When using the other two mapping schemes (LtoG_M1 and LtoG_M2) the assignment of boreal tree PFTs to shrub types is limited by a higher tree height threshold and partially because other PFTs (perennial grass) are substituted for cold shrubs. Regional patches of increased ground albedo and surface cooling over the higher latitudes of the Northern Hemisphere are also evident when using the LtoG_M1 and LtoG_M2 translation schemes.

Precipitation during the Northern Hemisphere summer monsoon season (JJAS; June-July-August-September) appears similar among the three mapping schemes, as the larger changes are confined to the equatorial regions. A drying pattern over Europe appears in all three translation schemes, but it is comparatively more substantial under LtoG_M0 and LtoG_M1 than LtoG_M2.

All translation schemes also lead to increased precipitation over equatorial South America. Annual mean river runoff for the Amazon River is simulated at 305, 297, and 308 km^3/month for LtoG_M0, LtoG_M1 and LtoG_M2, respectively, a slight improvement to the original Preindustrial (PI) run runoff of 280 km^3/month using the standard present-day land cover boundary condition. Compared to observations, ModelE2.1 shows a substantial deficit in Amazon River runoff in present-day simulations because of insufficient precipitation over the watershed (Fekete et al., 2001; Kelley et al., 2020).

Based on this evaluation of the different ways of translating LPJ PFTs to GISS PFTs, we found that LtoG_M2 was the scheme that simulates global precipitation and surface temperature most consistently with observations, and ground albedo that is closest to the standard pre-industrial boundary conditions dataset used usually used to drive ModelE. Figure 3 shows the difference in PFT cover fraction using LPJ-LMfire with the LtoG_M2 scheme compared to the standard ModelE boundary condition land cover data set for the late preindustrial time (PI; 1850 CE).

Compared to the ModelE standard land cover dataset for PI, LPJ-LMfire simulates increased extent and fraction of most trees (drought broadleaf, evergreen needleleaf, and evergreen broadleaf). Despite selecting a relatively high threshold for tree height to be classified as shrubs (up to 11 meters for both arid and cold types) the simulated cover fraction of shrubs is low compared to the standard PI land cover dataset for ModelE. The coverage of both annual and perennial C_3 grasses is greater in LPJ-LMfire in extratropical and polar regions. Similarly, C_4 grasses, which are not present in cooler climates, shows greater coverage in LPJ-LMfire in equatorial regions. LPJ-LMfire simulates some vegetation cover in the Sahara and Arabian deserts while the standard PI boundary conditions dataset suggests that most of this region is bare soil.

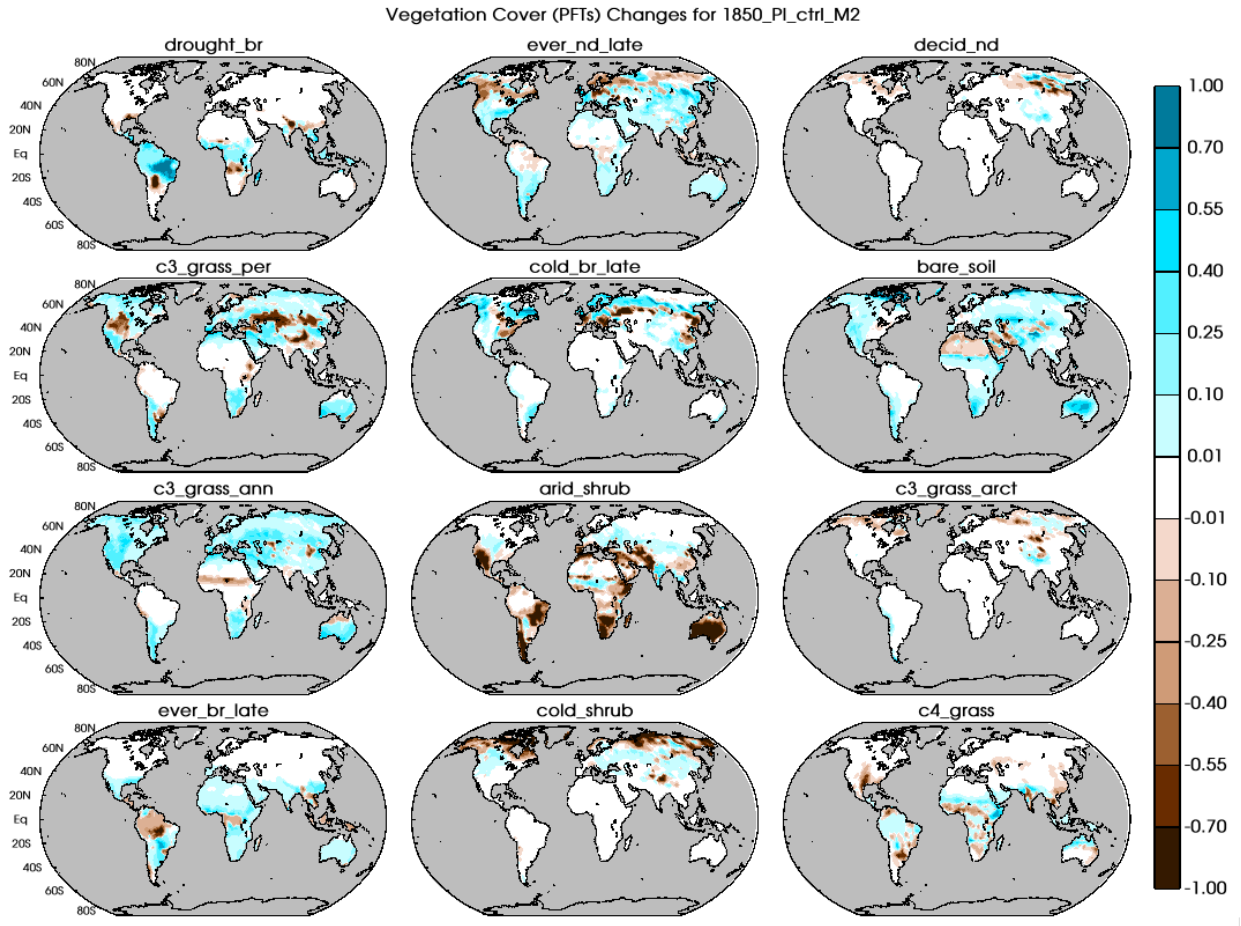

Figure 3. Differences between the LPJ-LMfire simulated vegetation distribution (PFTs and land cover type) and satellite-based land cover boundary conditions used in ModelE for the PI control period and the selected mapping schemes (LtoG_M2).

3.3 Vegetation Cover Changes under various combinations

We chose a set of five model configurations (Table 2) to quantify the model bias and interannual variability in our asynchronous coupling framework for the 2.5ka period. Supplementary figures S3, S4, S5, S6, and S7 show the spatial differences between prescribed land cover boundary conditions maps and land cover interactively simulated by our LPJ-LMfire-ModelE coupled model, which is henceforth referred to as the "coupled model system". These land cover difference maps are shown for each of the different model configurations described above, following the final iteration of the asynchronous coupling when the coupled model system is assumed to be either equilibrated or the process was truncated due to instability (Table 2). Supplementary figures S3, S4, and S5 show the changes in the land cover from the default ModelE land cover boundary conditions map for PI (Supplementary Fig S1); Supplementary figures S6 and S7 show the differences calculated from the modified vegetation following the PMIP4 protocols (Supplementary Fig S2).

Across all configurations, most of the tree PFTs show an increase in cover in the coupled model system relative to the prescribed land cover maps. However, in simulations where bias correction to the climate model was not applied, deciduous needleleaf tree cover is reduced in the high latitudes of the Northern Hemisphere (2.5k_PI_x_x, 2.5k_PI_x_GISS and 2.5k_GS_x_GISS) and this, in turn, has a substantial impact on regional climate. The coupled model system simulates increased annual and perennial C_3 grass cover across all configurations relative to the prescribed maps, while the Arctic C_3 grass shows a mixed regional response. Increased C_4 grass cover is mostly confined to the equatorial region and Southern Hemisphere; over the Northern Hemisphere C_4 grass cover decreases, irrespective of the inclusion and exclusion of interannual variability or bias correction. As discussed previously, the extent of arid and cold shrubs is reduced significantly in the coupled model system relative to the prescribed maps, even when the threshold height to separate trees from shrubs was set at a relatively tall limit of 11 m. A similar reduction in shrub cover relative to the land cover map used to initialize the simulation vegetation distributions is also simulated under all configurations.

In Figures 4 and 5 we present heatmap-type diagrams of the mean land cover fraction over selected regions to demonstrate and understand the pattern of change in vegetation distribution

simulated by the coupled model system. These figures depict changes in land cover under the different asynchronous coupling experimental configurations used in this study. Vegetation fraction change is averaged over northern Asia (NAS) (Fig. 4) and eastern Africa (Fig. 5; see Fig. 13 for the region boundaries; NAS: magenta; EAF: blue). Deciduous needleleaf tree cover over northern Asia (60°N-77°N, 70°E-135°E) is replaced by bare soil in all experimental configurations where bias correction of the climate model output was not applied. A similar disappearance of evergreen needleleaf late-successional forests, as well as a quick disappearance (within the first iteration) of cold shrubs, was also noticed. This suggests that, in the absence of bias correction, the model's drift towards colder conditions strongly influences vegetation growth in subsequent iterations over higher latitudes, which is inconsistent with the standard land cover boundary condition dataset used with ModelE (Kelley et al., 2020). On the other hand, when bias correction is applied along with interannual variability from either model (2.5K_PI_BC_LPJ and 2.5K_GS_BC_GISS), boreal forests are present in the northern Asia region along with cold shrubs and grasses.

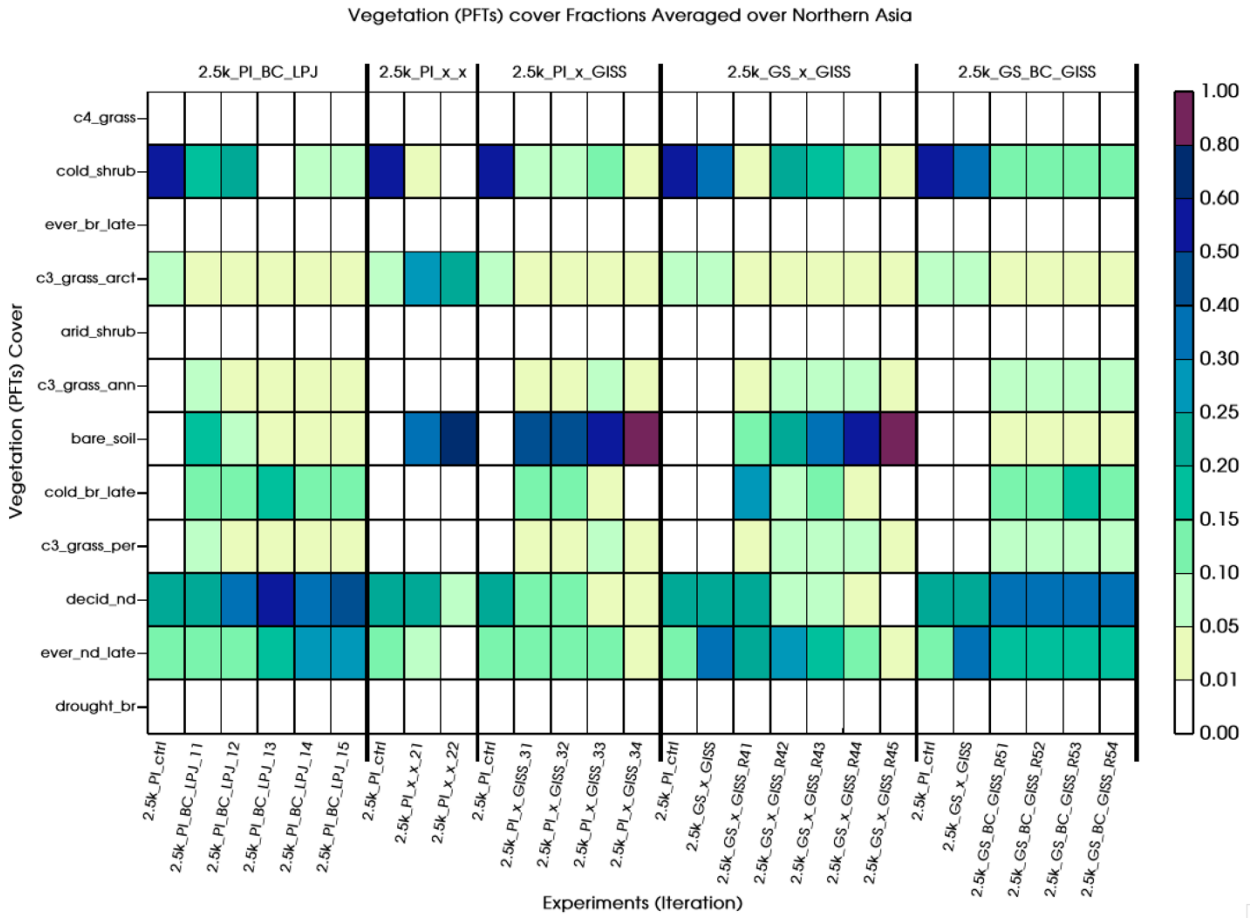

460

461 **Figure 4.** Area average of fractional land cover over Northern Asia region (60°N-77°N, 70°E-
462 135°E) under the range of experimental configurations used in this study.

463

464 Over eastern Africa (EAF: 0° N-18° N, 25° E-46° E) the impact of bias correction is less
465 important than over the high latitudes of the Northern Hemisphere. The presence of broadleaf
466 tree PFTs (drought broadleaf and evergreen broadleaf) and C_4 grasses is consistent across all the
467 experimental configurations used. However, the cover fraction of arid shrubs decreased
468 substantially, associated with a slight increase in the bare soil fraction.

469

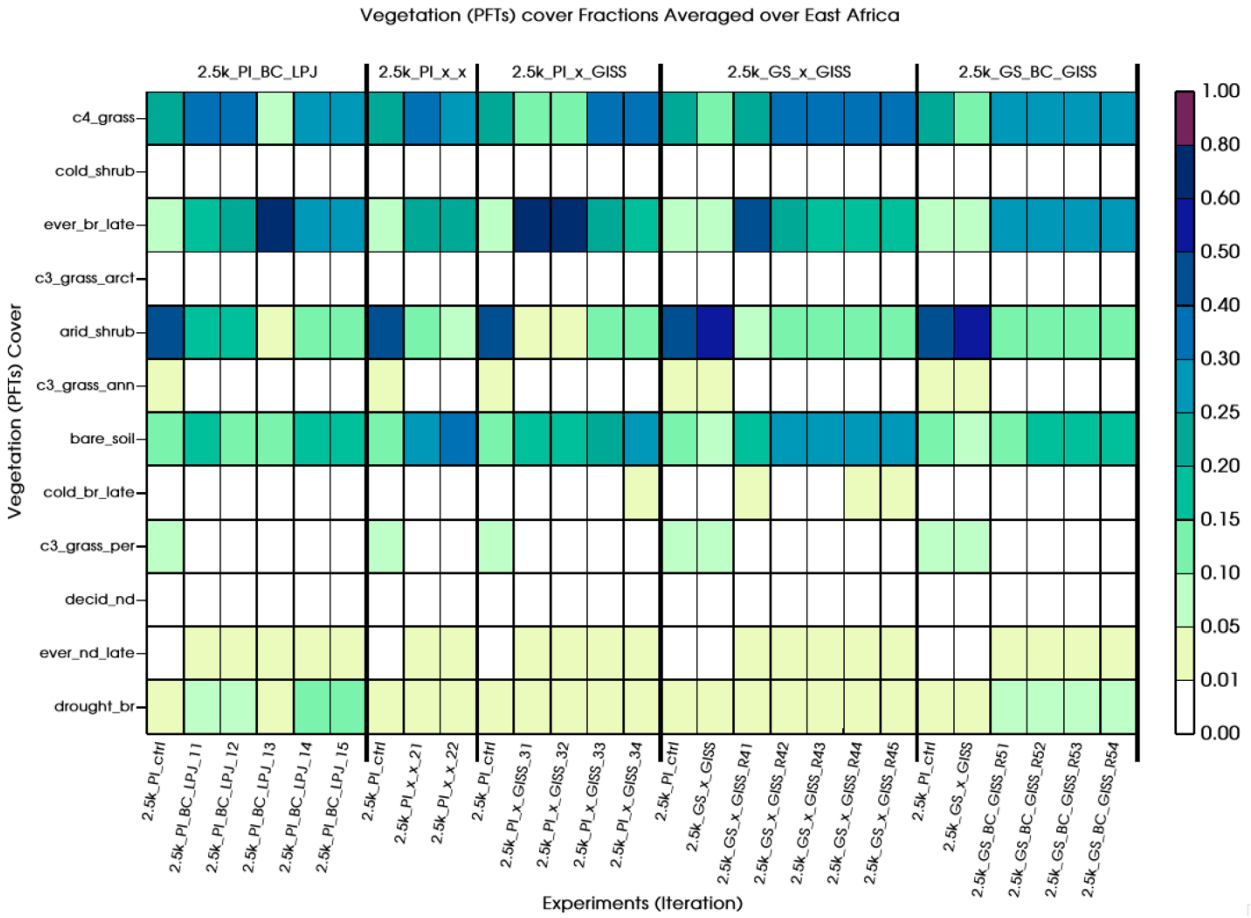

Figure 5. Same as Figure 4, but for Eastern Africa (0°N-18°N, 25°E-46°E).

4.0 Comparison with paleoclimate-proxy records for 2.5ka

To evaluate the coupled model system's skill in representing past climate, we compared our simulations for 2.5ka with multiproxy temperature reconstructions and speleothem-based oxygen isotope records.

4.1 Comparisons with reconstructed temperature

Kaufman et al. (2020) used five different statistical methods to reconstruct temperature at 1319 globally distributed sites covering part or all of Holocene from a range of proxy types. For each method, a 500-member ensemble of plausible reconstructions was presented. For comparison with our model output, we extracted temperature anomalies for 2.5ka (relative to the value reconstructed for the late preindustrial Holocene) from the ensemble reconstructions, which then binned into six latitude bands between the North and South Poles (each 30 degrees wide). We

computed the mean and median zonal anomaly using all 500 estimates of mean surface temperature (MST) over each band for each of the five methodologies (total 2500), along with the 5-95 percentile interval to represent uncertainty/variability among the sites in each zone and across reconstruction methods (black bar in Figure 6) as suggested by Kaufman et al. (2020).

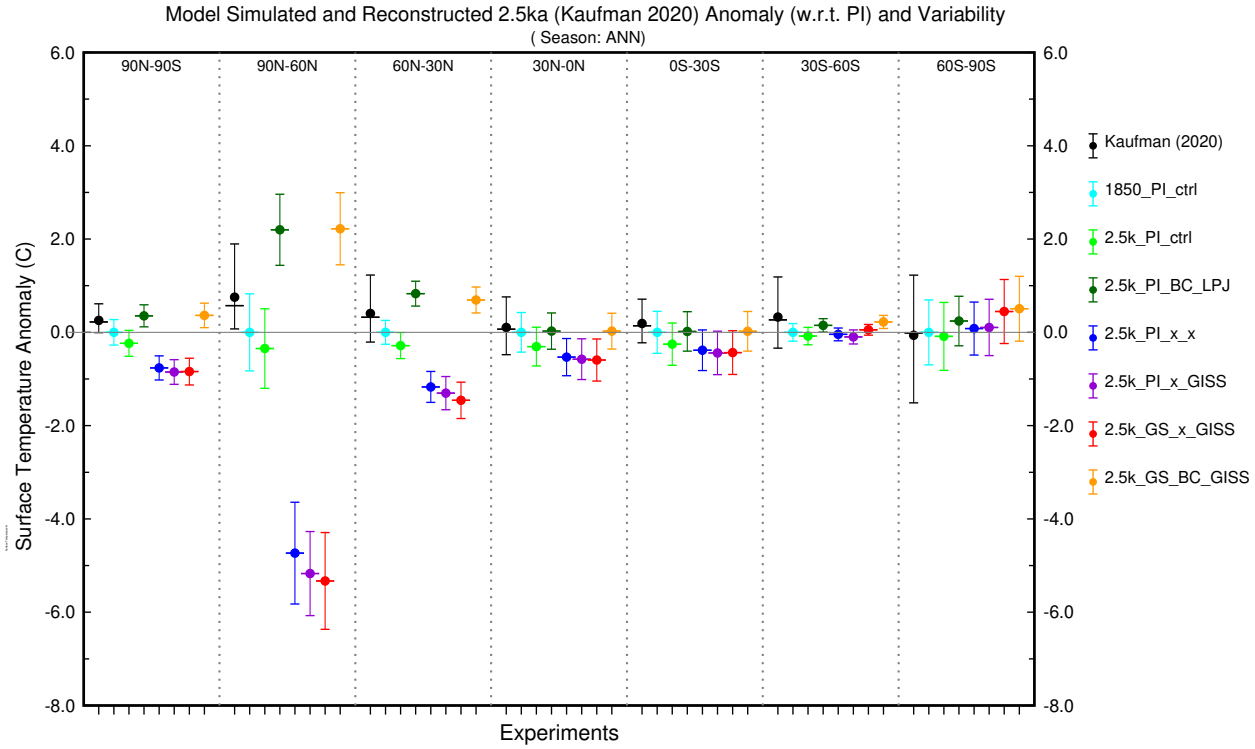

Figure 6: Comparison of model-simulated annual surface temperature anomalies and interannual variability for 2.5ka (with LPJ-LMfire vegetation) against independent proxy-based temperature reconstructions (black, Kaufman et al., 2020). Mean (circle), median (line) along with the 5-95 percentile range as variability bars (whiskers) and different colors that represent the final iteration of our different experiments.

Figure 6 shows that the 2.5ka control simulation with present-day vegetation is comparable to pre-industrial conditions (1850_PI_ctrl), exhibiting a slightly cooler climate. In contrast, proxy-based surface temperature reconstructions (Kaufman et al., 2020) indicate slightly warmer conditions at the global mean as well as across most latitude bands, except the far south (60S-90S). Applying bias correction allows the model to reproduce the same anomaly sign as the reconstruction, with minimal global (90N-90S) mean bias relative to the proxy data

(2.5k_PI_BC_LPJ and 2.5k_GS_BC_GISS). Although the magnitude of warming remains higher at the northern hemisphere high latitudes, this framework demonstrates the improved capability of the model to reproduce reconstructions through the incorporation of biogeophysical effects of past vegetation by adopting a bias correction. Model simulations where bias correction was not applied show colder conditions than the reconstructions globally and in the Northern Hemisphere. These differences between model and proxy are very large in the high latitudes of the Northern Hemisphere and statistically significant throughout the extra-tropics. In the Southern Hemisphere, the differences between model and proxy reconstructions are smaller and insignificant, and there is less difference between simulations with and without bias correction. It should be noted that the larger uncertainty in reconstructed temperature over the southern polar band is due to a noticeably lower number of available proxy records (157 records; Kaufman et al., 2020).

4.2 Comparisons with speleothem oxygen isotope ratios

The isotopic composition of oxygen in water, expressed as the ratio of ^{18}O to ^{16}O serves as a fundamental tracer for investigating changes in the hydrological cycle. This ratio is highly sensitive to regional climate conditions and to the processes that regulate the hydrological cycle, such as temperature, precipitation, and evaporation. ModelE2.1 includes a representation of the stable water isotopologues as passive tracers and the isotopic composition of precipitation can be diagnosed from the model output (Aleinov and Schmidt, 2006; LeGrande and Schmidt, 2006; Schmidt, 1998). We compared the simulated mean annual isotopic composition of precipitation ($\delta^{18}O_p$) with oxygen isotope records from the Speleothem Isotope Synthesis and Analysis (SISAL) version 2 database (Comas-Bru et al., 2020). Using the published chronologies for each speleothem record we extracted all samples dated between 3-2 ka, which resulted in 163 measurements from 111 sites. Depending on their mineralogy (i.e., calcite or aragonite), the mean $\delta^{18}O$ values (VPDB) were converted to their drip water equivalents that could be compared to simulated $\delta^{18}O_p$ (VSMOW) (Comas-Bru et al., 2020). We used simulated mean surface air temperature obtained from the grid points nearest each cave site to estimate the cave temperature required to convert mineral $\delta^{18}O$ to an equivalent the drip water value. For each of our model experiments, we extracted simulated $\delta^{18}O_p$ nearest to each cave site and compared it with the estimated drip-water $\delta^{18}O$.

Overall, the mean $\delta^{18}O_p$ spatial distribution in all 2.5ka simulations is in excellent agreement with the proxies, showing better pattern correlations (r_{pat}) than 0.83 (Figure 7), with the 2.5k_PI_x_x iteration marginally showing the highest skill (i.e., r_{pat} = 0.85 and RMSE = 1.90; shown in supplementary Fig S8). For comparison, the worst simulation using this metric, 2.5k_GS_BC_GISS, is almost as equally skillful (r_{pat} = 0.84 and RMSE = 1.92; Supp. Fig. S8), demonstrating that none of the different configurations we presented here were significantly different.

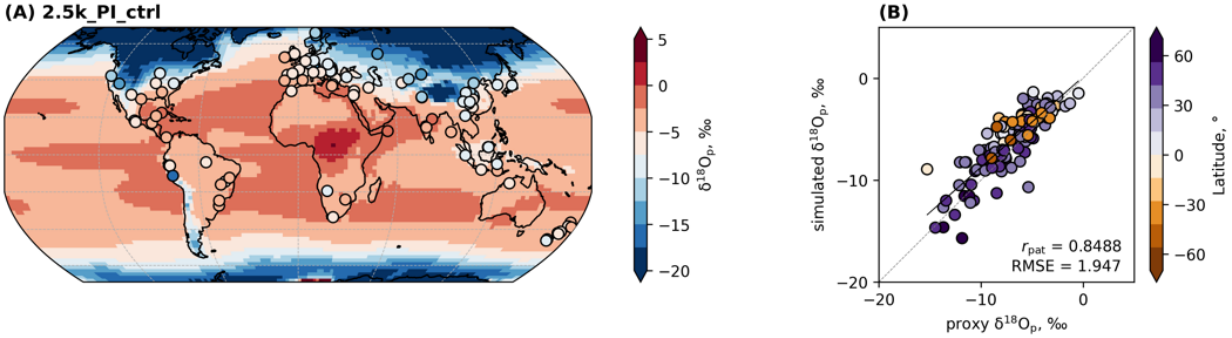

Figure 7. Comparison of simulated $\delta^{18}O_p$ with speleothem $\delta^{18}O$. Left: global distribution (70° S-70° N) of simulated $\delta^{18}O_p$ (background) and speleothem $\delta^{18}O$ (circles), converted to their drip water equivalents (see main text) for the 2.5k_PI_ctrl simulation. Right: scatterplots between simulated and proxy $\delta^{18}O_p$. Black line represents the least squares regression fits to data points, while the gray dashed line represents the 1:1 line. r_{pat} and RMSE are reported in the lower right corner of the scatterplot. For comparison against each model experiment, see Fig. S8.

Regionally, we similarly found that most simulations show no significant deviation with each other (Figure 8, Figure 9). We note, however, that over Europe (Figure 9E), variability may be explained by the observed change in magnitude on both SAT and summer precipitation among simulations (further sections). Over India and Central Asia (Figure 9F), simulations with bias correction show lower correlation and higher RMSE values compared to other models against proxy $\delta^{18}O_p$. This is likely related to the observed increase in mean summer precipitation over this region that was not reflected in the proxy sites.

Compared to proxy $\delta^{18}O_p$, simulations over certain regions show better agreement. Europe, which is the most densely sampled region, show the best agreement with the proxies (i.e., high

correlation, closest to the reference point, Figure 9E), and with the 2.5k_PI_x_GISS iteration best capturing the spatial $\delta^{18}O_p$ pattern (i.e., r_{pat} = 0.94 and RMSE = 1.26). In contrast, simulations over Central America, South America and Africa show the least skill where the magnitude of $\delta^{18}O_p$ change is consistently underestimated (i.e., moderate to high correlation but farthest away from the reference point). This may largely be due to inadequate sampling in these regions, especially for Africa, and/or both precipitation and SAT influencing $\delta^{18}O$ may be underestimated at these proxy locations, resulting in a generally muted $\delta^{18}O$ response across simulations. Cave-specific factors that alter speleothem $\delta^{18}O$, for example, groundwater mixing or fractionation (Baker et al., 2019; Hartmann and Baker, 2017; Lachniet, 2009) are also not effectively reproduced in the models, contributing to the proxy-model mismatch. Regions where the largest simulated SAT, precipitation, and $\delta^{18}O_p$ change relative to the 2.5k_PI_ctrl are observed, such as northern Africa, the Amazon basin and Siberia, are not adequately represented by reconstructions, highlighting the need to expand the proxy network to marine-based records and polar regions over the period of interest to capture the full range of isotopic variation.

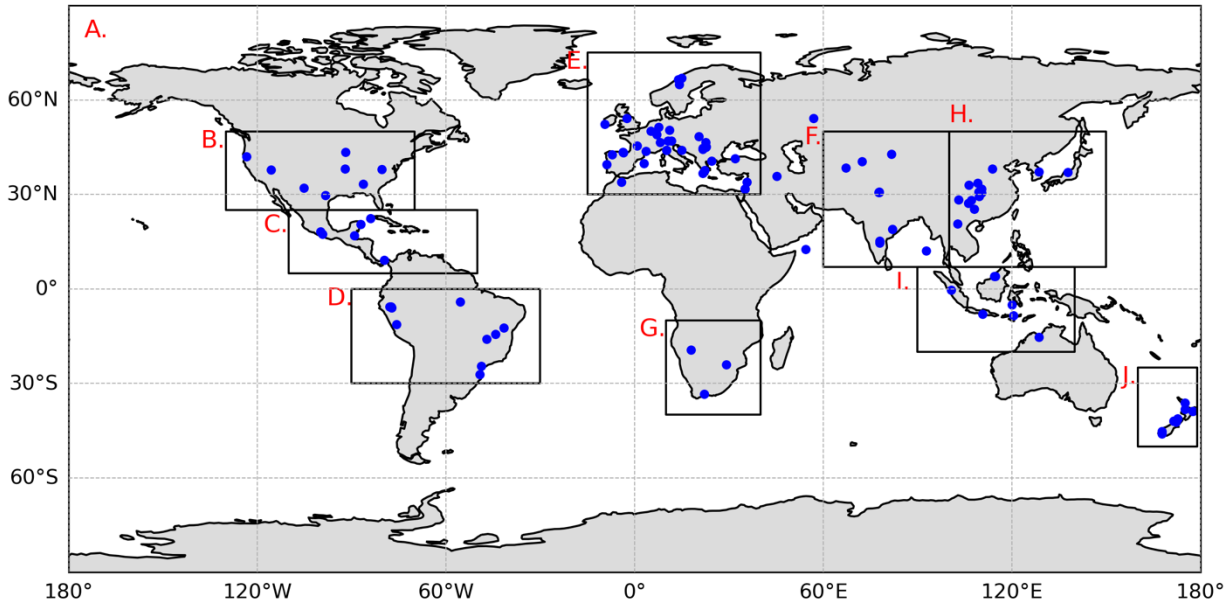

Figure 8. Demarcation of geographical regions described in the main text. Labels A to J correspond to the respective Taylor diagram plots in Figure 9.

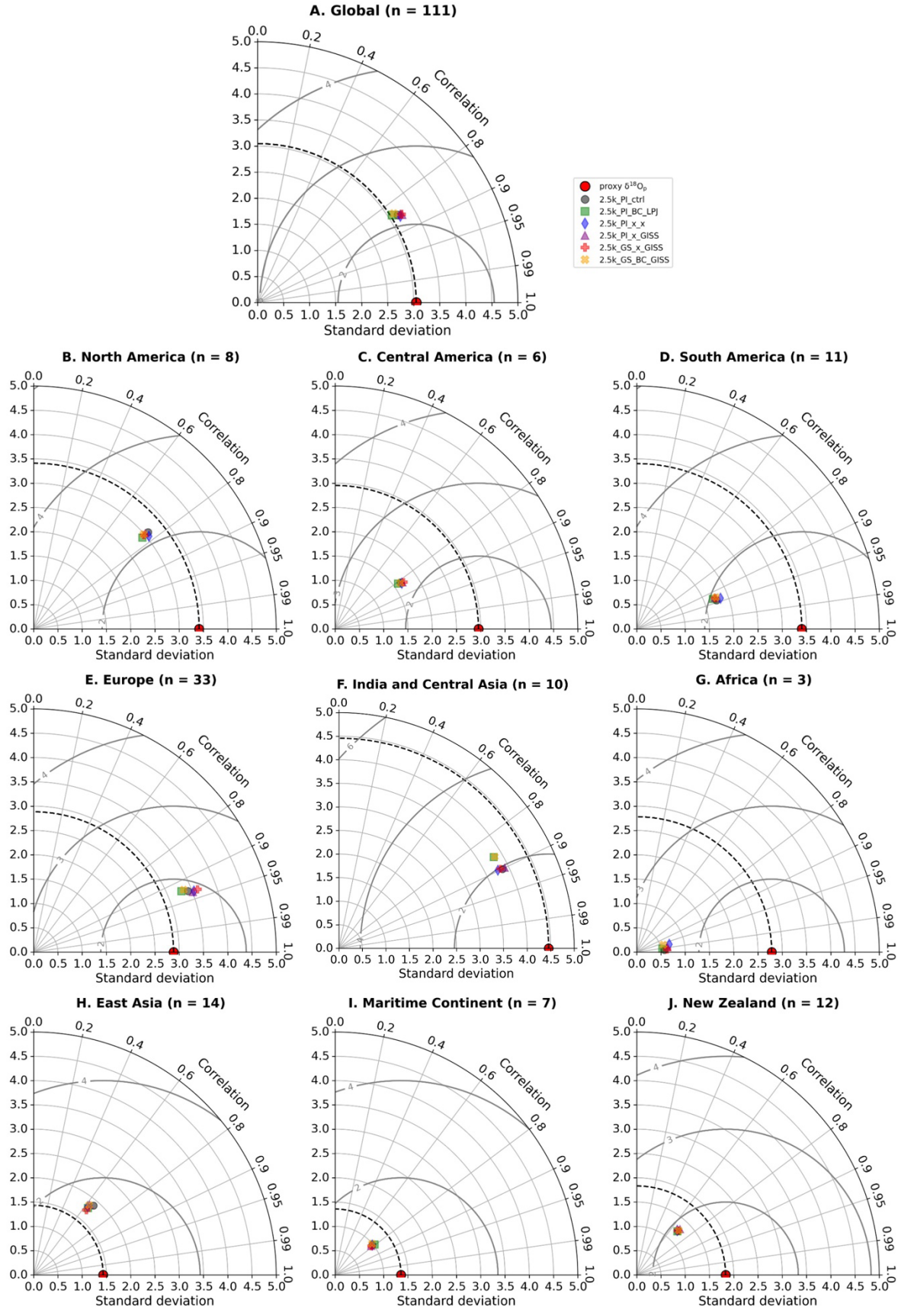
A. Global (n = 111)
B. North America (n = 8)
C. Central America (n = 6)
D. South America (n = 11)
E. Europe (n = 33)
F. India and Central Asia (n = 10)
G. Africa (n = 3)
H. East Asia (n = 14)
I. Maritime Continent (n = 7)
J. New Zealand (n = 12)
Correlation
Standard deviation
proxy $\delta^{18}O_p$
2.5k_PI_ctrl
2.5k_PI_BC_LPJ
2.5k_PI_x_x
2.5k_PI_x_GISS
2.5k_GS_x_GISS
2.5k_GS_BC_GISS

575

Figure 9. Taylor diagrams showing the r, SD and RMSE values between the proxy-derived and simulated $\delta^{18}O_p$ for each 2.5k iteration globally (A) and at each subregion (B to J). The sub-regions are shown on the map in figure 8.

5.0 Global climate response

To evaluate the spatial features of the equilibrium climate simulated by ModelE, we analyzed the last 100 years of the final iteration of each coupled model system experimental configuration. We aimed to understand the biogeophysical feedback due to vegetation cover changes as well as the role of model configuration on climate. Figure 10 shows surface albedo (%) for ModelE in its initial PI state, and differences between this initial state and simulated albedo for 2.5ka using the coupled model system. We used student's t-tests to estimate if the albedo differences were statistically significant at the 95% confidence level. The coupled model system shows substantial vegetation cover change over the high latitudes of the Northern Hemisphere. As expected, most of the significant changes occur over land, while changes in albedo over the oceans are largely insignificant. The spatial pattern of albedo change differs between simulations where bias correction was applied (2.5k_PI_BC_LPJ and 2.5k_GS_BC_GISS) and those where it was not (2.5k_PI_x_x, 2.5k_PI_x_GISS, and 2.5k_GS_x_GISS). Albedo over the high latitudes of the Northern Hemisphere decreases up to 10% caused by increased tree cover fraction (deciduous needleleaf and evergreen needleleaf) in the coupled model system relative to standard PI land cover dataset.

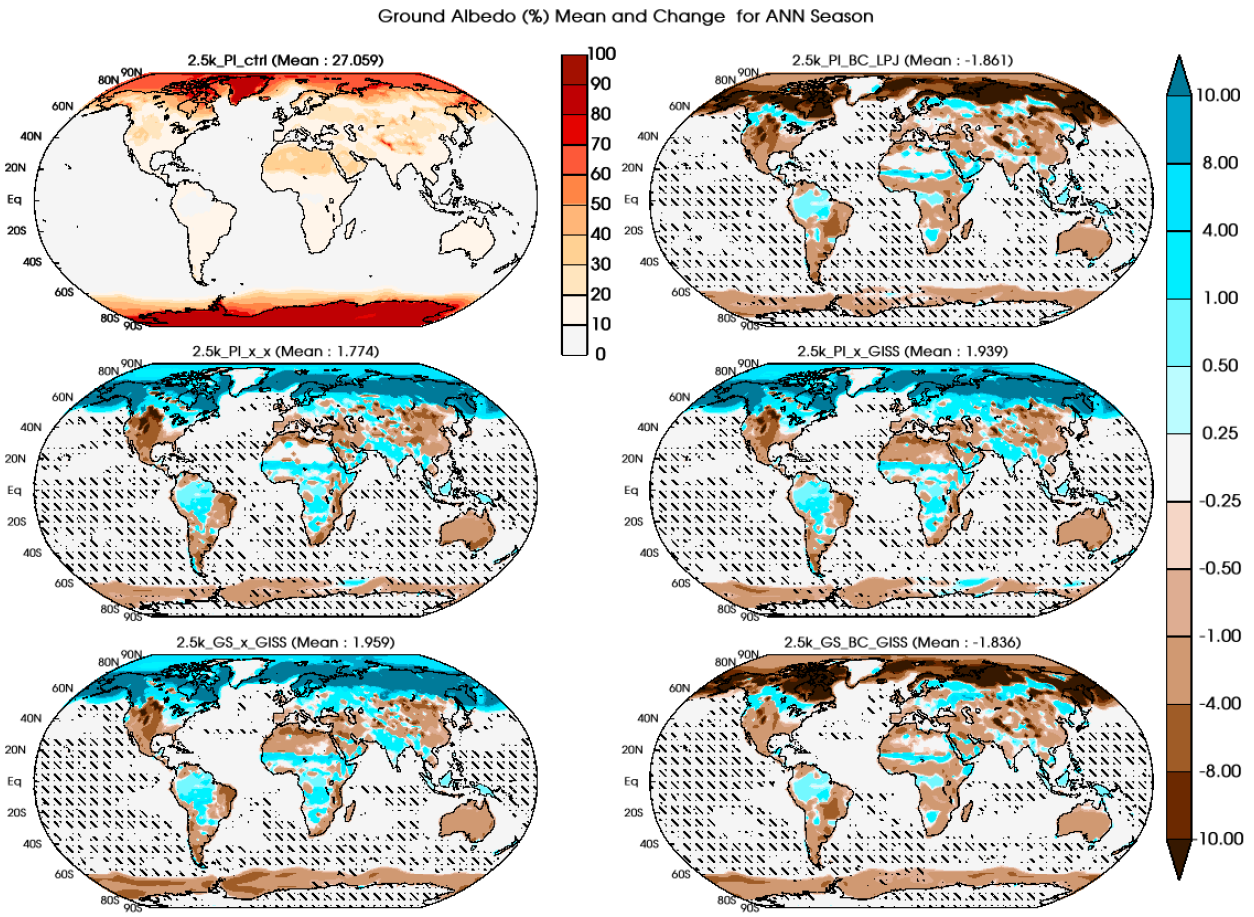

Figure 10. Annual mean (top left; 2.5k_PI_ctrl) and change (all other panels) of surface albedo (%) for the final iteration of various experiment configurations listed in Table 2. Stippling indicates the region over which change is not statistically significant at a 95% confidence level (using the student's t-test).

This increased tree cover fraction subsequently absorbs more incoming solar radiation and raises surface temperature by 2-4 °C over high latitude regions compared to the control run (Fig. 11 top-right and bottom-right panels). In experiments where bias correction was not applied (2.5k_PI_x_x, 2.5k_PI_x_GISS and 2.5k_GS_x_GISS), the relatively cold conditions simulated by the coupled model system shows an opposite albedo-vegetation response (> 3 °C cooling over Northern Hemisphere high latitudes). This drift towards a colder climate in the absence of bias correction resulted in the continuous formation of sea ice that ultimately reaches the (shallow) seabed, effectively creating land ice and eliminating the ocean from the grid cell. In coupled model system experiments without bias correction, we terminated the iterative processes when

this freezing of the ocean to the seabed occurred, because this condition caused the model to crash (2.5k_PI_x_x, 2.5k_PI_x_GISS, and 2.5k_GS_x_GISS).

At lower latitudes, albedo tends to show decreases relative to the standard boundary conditions in all experiments, particularly over the forested areas of the equatorial regions and temperate latitudes of the Northern Hemisphere. Over northern Africa and the Indian subcontinent, changes in both albedo and surface temperature are more mixed. Albedo change in central and northern Africa are driven by a reduction in the area occupied by shrubs and an increase in bare soil fraction. This pattern of increased albedo is more prevalent in simulations that were initialized with Green Sahara land cover boundary conditions.

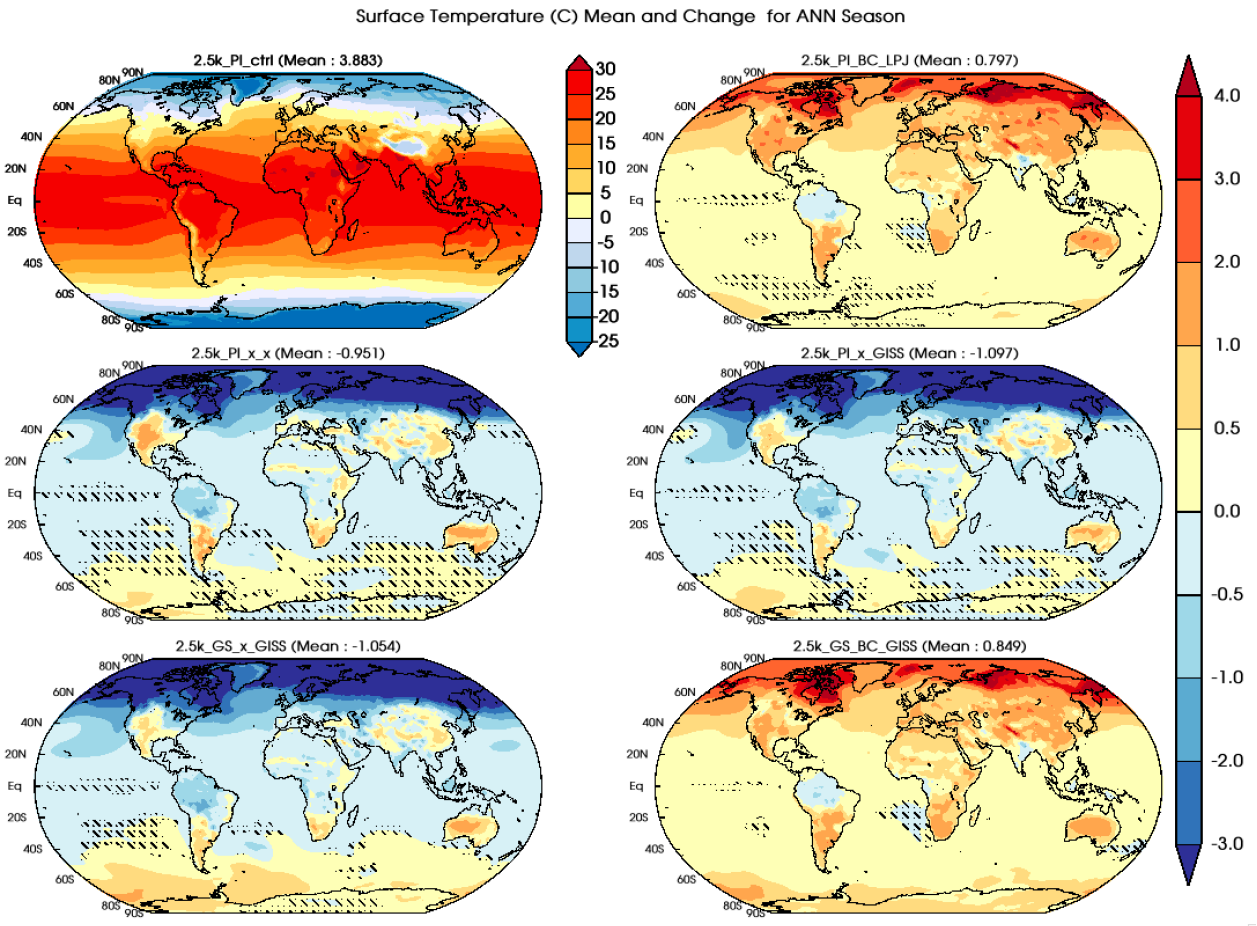

Figure 11. Same as figure 10 for Surface air temperature (°C) mean and change on an annual scale (ANN season).

In experiments that were initialized with “Green Sahara” land cover boundary conditions where interannual variability from GISS ModelE is included with and without adopting the bias correction, comparison of the surface temperature response between simulations with (2.5k_GS_x_GISS; Figure 11, bottom-left) and without bias correction (2.5k_GS_BC_GISS; Figure 11, bottom-right) reveal the significance of bias correction for the asynchronous coupling process. Broadly, we can observe that bias correction induces a warming of 0.7-0.8 °C, and exclusion leads to a cooling of 0.9-1.1 °C, at the global scale, predominantly over the northern hemisphere land regions.

Precipitation change across the model configurations is shown for Northern Hemisphere summer (JJAS) at global scale in Figure 12. The significance of bias correction is noticeable over the high latitudes of the Northern Hemisphere. Simulations with bias correction (2.5k_PI_BC_LPJ, 2.5k_GS_BC_GISS) lead to an increase in JJAS season precipitation relative to the initial boundary conditions, while those experiments without bias correction (2.5k_PI_x_x, 2.5k_PI_x_GISS) show reductions in precipitation. Reductions in precipitation relative to initial conditions are visible in Europe in all configurations and are greater in experiments where bias correction was not applied. Another common feature among the experiments was the variable spatial pattern of JJAS precipitation change over tropical regions. All configurations showed increased precipitation over south and east Asia. Over the Nile headwaters in East Africa (Melesse et al., 2011) precipitation increased, particularly in those experiments where bias correction was applied. Interestingly, increased Northern Hemisphere summer monsoon season (JJAS) precipitation over the Asian continent was simulated across all configurations. In contrast, only a marginal northward procession of ITCZ over tropical Africa was simulated.

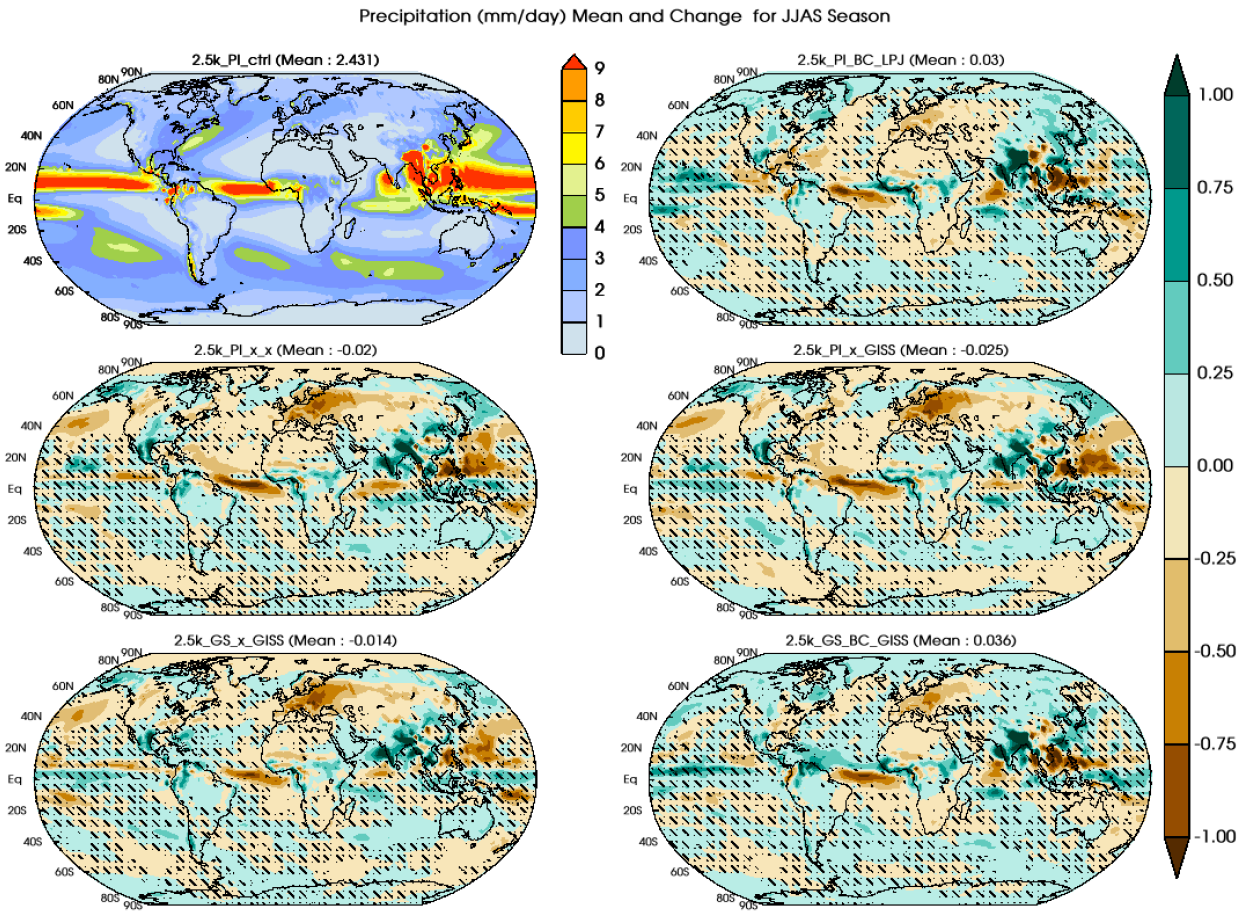

Figure 12. Same as figure 10 for precipitation (mm/day) mean and change for the JJAS season.

5.1 Regional climate

The spatial pattern of changes in climatic features for 2.5ka using our coupled model system shows several prominent and robust regional signatures of climate change. We selected nine regions over land (Fig. 13; Table 3) to analyze regional temperature and precipitation changes in our simulations. Area-averaged time-series anomalies with respect to the 2.5ka control run (2.5k_PI_ctrl) for the various experiments performed are calculated for these different regions.

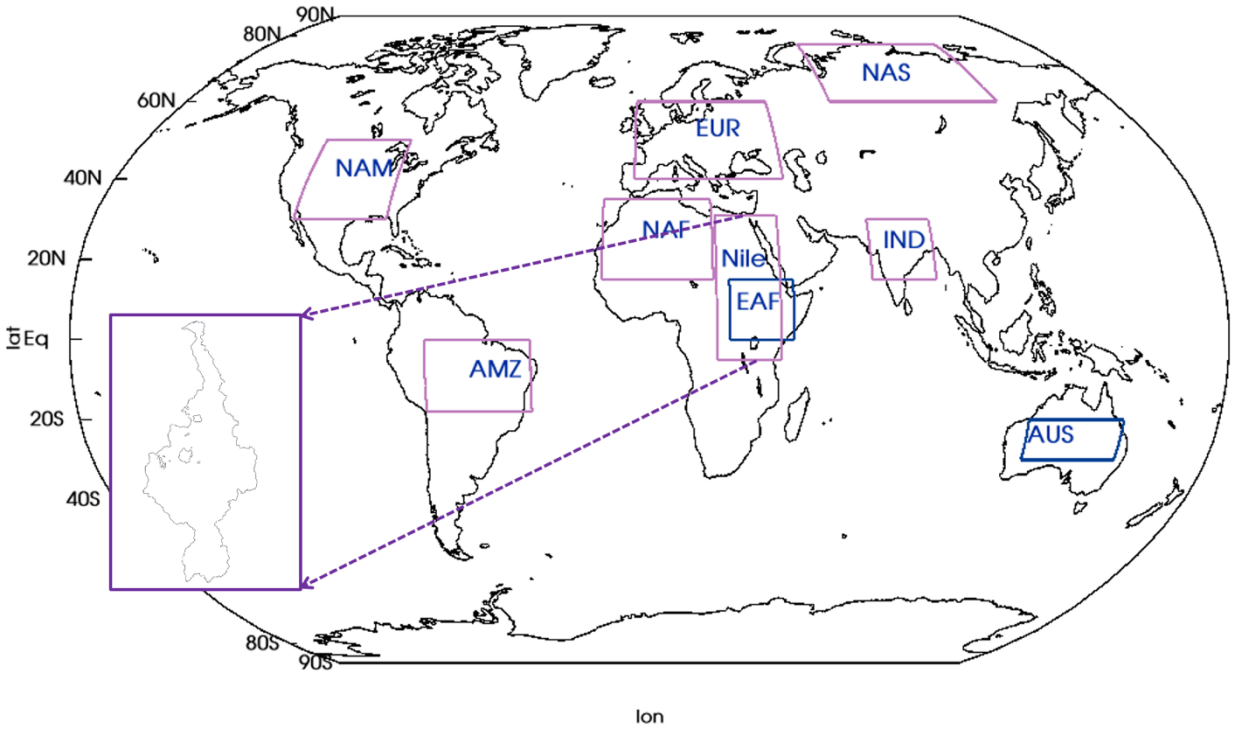

Figure 13. Boundaries for the regions used for regional analysis. The inset map shows the Nile River basin in high resolution, which is superimposed upon the ModelE resolution to generate the grid-specific weights for the Nile River basin. The EAF and AUS regions are used in Figs. 4, 5 and 15.

Table 3: - Region details including the boundary coordinates for all the regions.

Region (long name)	Region (short name)	Region boundary (Latitudes)	Region boundary (Longitudes)
North America	NAM	30°-50° N	115°-85° W
Amazon Rainforest Region	AMZ	0°-18° S	37°-70° W
Northern Asia	NAS	60°-77° N	70°-135° E
North Africa	NAF	15°-35° N	15° W-20° E
Europe	EUR	40°-60° N	5° W-45° E
Indian Region	IND	15°-30° N	70°-90° E
Nile River Basin	Nile	5° S-31° N	21°-41° E
East Africa	EAF	5°-15° N	25°-45° E
Australia	AUS	20°-30° S	120°-150° E

Figure 14 shows box-and-whisker plots of mean and median annual surface temperature (top) and JJAS seasonal precipitation (bottom) change, as well as the 5-95 percentile range (interannual variability) along with the upper and lower quartiles (25^{th} and 75^{th} percentiles) of the anomaly time series for each region. As suggested from the global analyses of spatial patterns, the shift towards relatively warmer or colder climate as a result of applying bias correction is evident. Bias correction leads to a pronounced warming over northern Asia (NAS region) of 3-4 °C, while without bias correction this region cools by 5-6 °C. The partition between experiments with and without bias correction is also apparent over selected regions of the mid-latitudes between 35°-60° N (NAS and EUR).

Except for northern Asia (NAS), all regions show approximately similar interannual variability in mean annual surface temperature. In northern Asia interannual variability is greater, especially in simulations where bias correction was not applied. Our results show that interannual variability in summer temperature in northern Asia is sensitive to changes in land cover, with greater variability in simulations where bias correction was not applied.

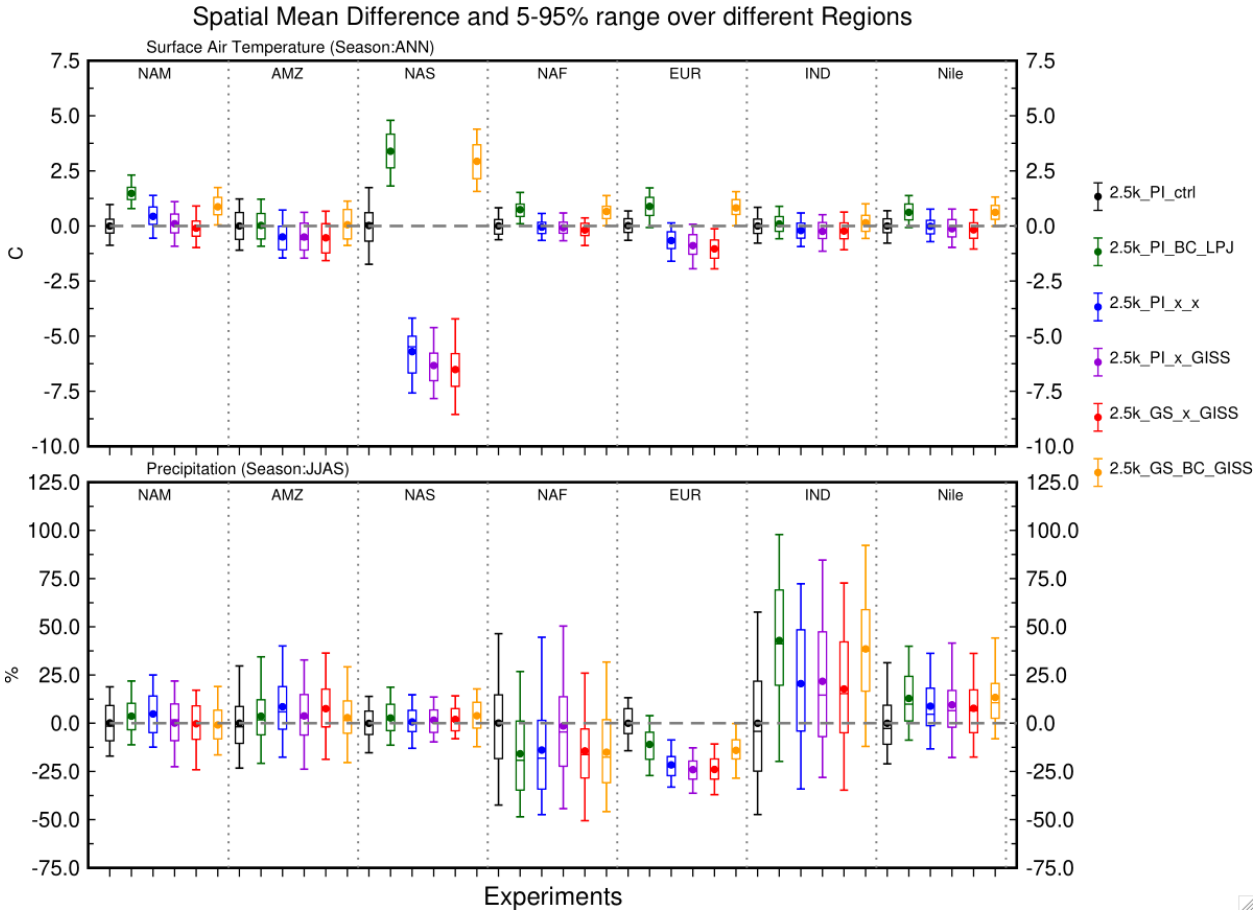

Figure 14. Regional change in surface air temperature (top panel, °C, annual mean) and precipitation (bottom panel, %, JJAS) for the various simulations with respect to the 2.5ka control run (2.5k_PI_ctrl). Regions as listed in table 3.

Simulated 2.5ka precipitation for the Northern Hemisphere summer (JJAS) shows substantial changes in mean state relative to the 2.5ka control with PI vegetations, particularly for the tropical regions of northern Africa, India, and the Nile basin (Fig. 14, bottom panel). Interannual variability in precipitation is comparable to the initial control run (black line). However, the magnitude of variability differs across the regions; it is more prominent in tropical regions than in the extra tropics. An increase in mean precipitation on the order of 20-30% without bias correction and up to 40% with bias correction is simulated in JJAS season precipitation for the Indian summer monsoon region (IND) and it is in a range of 10-25% increase over the Nile basin region. A drying pattern over Europe (EUR) ranges from 10-25% and is consistent for all the

simulations; a greater decrease in European precipitation was simulated when bias correction is not adopted. A similar drying pattern was also simulated over the North America (NAM) and northern Africa (NAF) regions. The relatively small magnitude of interannual variability in precipitation over Europe and North America suggests that our model does not produce high variability across these regions and that it is not sensitive to the different experimental configurations. Despite the large changes in both mean state and variability in temperature, precipitation over northern Asia (NAS) changes little from the control state and across simulations. In the Amazon region (AMZ), precipitation changes were small and not significantly different between simulations. Without bias correction, the coupled model system suggests a modest increase in mean seasonal precipitation of up to 10%. We also noticed a similar response of slightly increased precipitation in Southern Hemisphere summer (DJF) over Australia (not shown here).

We further investigated the way our experiments influenced the seasonal cycle of temperature and precipitation over the regions discussed above. Our results show that the seasonal cycle of surface temperature is broadly similar across experiments for all the equatorial regions except the Amazon (AMZ) region, where surface temperature is reduced by 0.5 °C in experiments where bias correction was not applied (Supplementary Fig. S9). Over the northern Asia (NAS) region, we see a considerable difference in the seasonal cycle of temperature of 5-15 °C between runs with and without bias correction. The seasonal cycle of temperature in the 2.5ka control (2.5k_PI_ctrl) simulation over NAS is intermediate to the experiments but tracks closer to the simulations where bias correction was applied, particularly in Northern Hemisphere winter, where, as noted above, simulations without bias correction result in very cold conditions in this region.

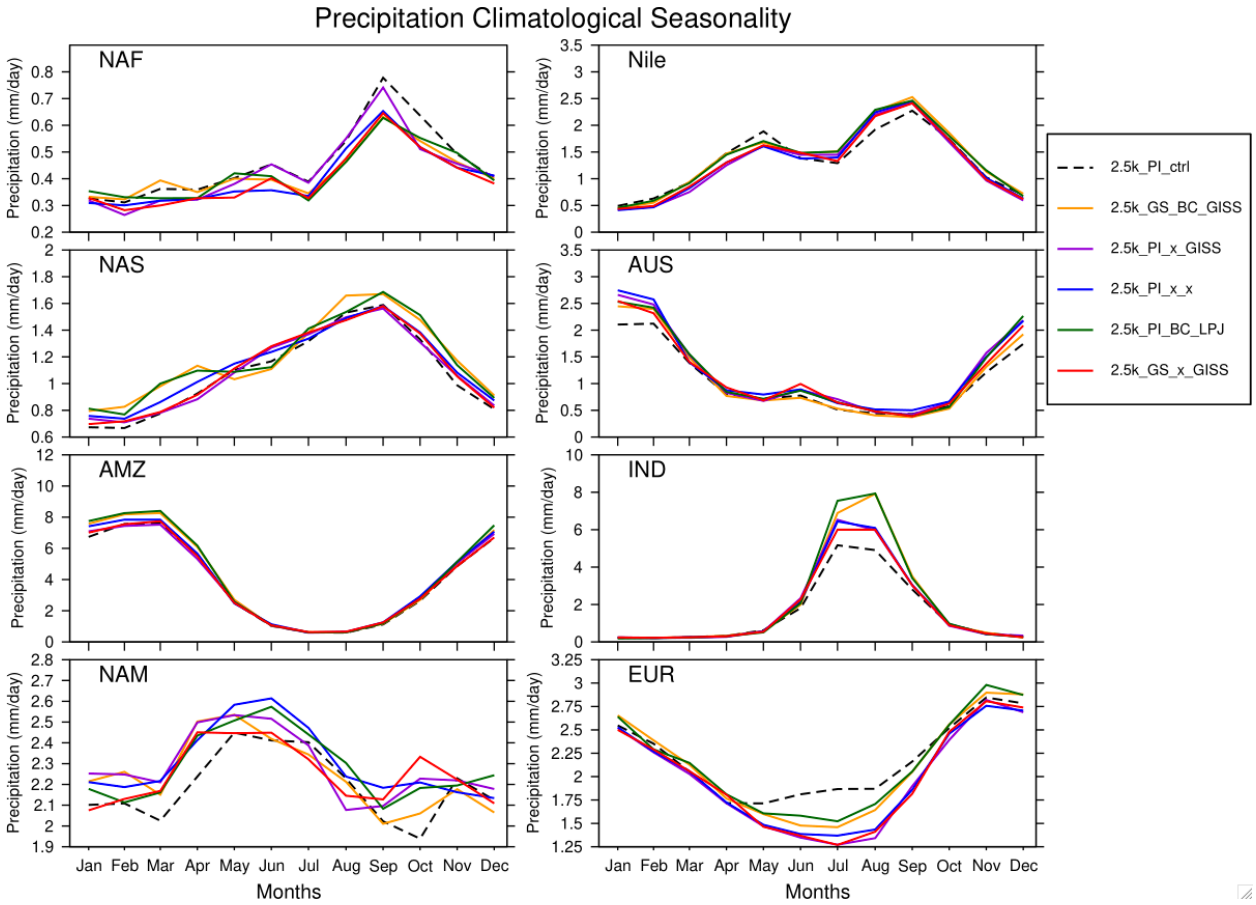

Figure 15. Seasonality of precipitation averaged over the selected regions for the final iteration of each experiment listed in table 2.

Compared to temperature, the seasonal cycle of precipitation shows greater differences among simulations over several of the regions (Fig. 15). An increase of 2-3 mm/day over the Indian region (IND) is simulated during the Indian Summer Monsoon months (JJAS) when using LPJ-LMfire-generated land cover for both types of experiments (with and without bias correction), with the bias-corrected simulations showing a larger increase in precipitation than the non-bias-corrected ones. When bias correction is applied, the seasonal peak of precipitation shifts from July to August. Over Europe, we observe a decrease of up to 0.5 mm/day in summer precipitation relative to the control simulation in all simulations that use the LPJ-LMfire PFTs. Precipitation decreases even more when the bias correction was not applied. The North Africa region (NAF) also shows a slight decrease in precipitation relative to the control over most of the seasonal cycle, while in North America (NAM) we see an increase in precipitation outside of the JJAS summer months. The Amazon rainforest region (AMZ) shows no change in the seasonal

cycle of precipitation in all experiments. The Nile River basin (Nile) and Australian (AUS) regions also show small increases in precipitation relative to the control in their respective monsoon seasons (JJAS and DJF). Overall, the changes in annual precipitation cycle (increases or decreases) over the studied regions are primarily driven by both the pole-equator thermal gradients in the various experiments, as well as the biogeophysical effects associated with regional vegetation changes over these regions (e.g. Indian Summer monsoon, North American and European region) (Pausata et al., 2014; Tiwari et al., 2023; Singh et al., 2023).

6.0 Discussion and Conclusions

Here we presented a generalized technical framework for asynchronously coupling a climate model (NASA GISS ModelE2.1) with a dynamic vegetation model (LPJ-LMfire), i.e., the "coupled model system", and demonstrate its skill in reconstructing climate in the late preindustrial Holocene and for 2.5ka. We examined the role of bias and interannual variability corrections in this process, and showed how they influence simulated land cover and climate. We demonstrated the importance of considering such metrics in such a framework in our experimental design and global and regional scale analyses. We performed a detailed evaluation and comparison of the climate simulated by the coupled model system with reconstructions of air temperature (Kaufman et al., 2020) and the isotopic composition of precipitation ($\delta^{18}O_p$) based on speleothems (Comas-Bru et al., 2020). Similarly to previous studies that used asynchronous coupling to simulate regional and global paleoclimate (Claussen*, 2009; Kjellstroem et al., 2009; de Noblet et al., 1996; Strandberg et al., 2011, 2014b; Texier et al., 1997; Velasquez et al., 2021), we assessed the influence of the biogeophysical feedback between land and atmosphere.

Our results demonstrate the pronounced influence of including bias correction when passing simulated climate to the land surface model. To correct biases inherent in the climate model, in selected experiments we passed climate anomalies relative to a control simulation to the land model that were added to a standard baseline climatology based on contemporary observations. In simulations without this bias correction, raw simulated climate was passed directly from ModelE to LPJ-LMfire. Where bias correction was applied ModelE drifts towards warmer climate; simulations without bias correction drift towards colder climate. This effect was especially apparent in the high latitudes of the Northern Hemisphere, particularly over Asia. With bias

correction, high latitude vegetation is dominated by tree plant functional types, while without it, cold shrubs and arctic grasses are the predominant form of land cover. These results are characteristic of the well-known vegetation-albedo feedback that is important at high latitudes (Charney et al., 1977; Charney, 1975; Doughty et al., 2012, 2018; Pang et al., 2022; Stocker et al., 2013; Swann et al., 2010; Zeng et al., 2021).

The effects of bias correction on precipitation were less apparent and confined to regional scale. We simulated a greater Indian summer monsoon season (JJAS) precipitation with bias correction (>1 mm/day), and a nominal increase of ~0.5 mm/day across east China, Africa, and the North American monsoon region. In other regions, the patterns of precipitation change were similar across all experiments except for Europe where drier conditions are simulated in summer (up to –1 mm/day) in simulations where bias correction was not applied.

The high latitudes of the Northern Hemisphere were also the region with the largest disagreement between model and independent, multi-proxy temperature reconstructions. These comparisons also highlighted the important role of bias correction; experiments with correction were much more similar to reconstructions than those without. Simulations of the isotopic composition of precipitation ($\delta^{18}O_p$) shows an excellent agreement with speleothem records with a pattern correlation greater than 0.8. However, the difference in the magnitude of model simulated $\delta^{18}O_p$ from proxies over various regions indicates an underestimation of relationship between surface temperature and $\delta^{18}O_p$ variability (Henderson et al., 2006; Kurita et al., 2004). A global evaluation of model skill is hindered by the difference in the number of independent paleoclimate reconstructions available for different regions, particularly in north Asia where we see the greatest sensitivity of the coupled model system to the experimental setup. When examining modeled and reconstructed $\delta^{18}O_p$, in Europe, which is the region with the greatest number of records, we see a robust pattern correlation with lower RMS values as compared to other regions.

In this study, we confirmed the importance of the land surface for simulating paleoclimate, even for the late Holocene where land surface conditions were not as different from present as they were during, e.g., the last glacial cycle or even mid-Holocene (6ka). We demonstrated that asynchronous coupling can be a computationally inexpensive way of capturing land-atmosphere feedbacks and

improving the fidelity of the simulated climate. We noted that correcting bias present in the climate model is essential for simulating climate that is consistent with independent reconstructions, particularly for the high latitudes of the Northern Hemisphere. Future work with the coupled model system will include quantification of the influence of major volcanic eruptions for regional and global paleoclimate and the influence of past climate on the dynamics of complex civilizations in prehistory.

Code/Data availability

Details to support the results in the manuscript are available as supplementary information provided alongside the manuscript. GISS Model code snapshots are available at https://simplex.giss.nasa.gov/snapshots/ (National Aeronautics and Space Administration, 2024), LPJ-LMfire (https://zenodo.org/records/5831747), and important codes, calculated diagnostics as well as other relevant details are available at the Zenodo repository (https://doi.org/10.5281/zenodo.13626434) (Singh et al., 2024). However, raw model outputs, data and codes are available on request from author due to the large data volume.

Acknowledgements

RS, KT, ANL and FL acknowledge support by the National Science Foundation under Grant No. ICER-1824770. ANL acknowledges institutional support from NASA GISS. Resources supporting this work were provided by the NASA High-End Computing (HEC) Program through the NASA Center for Climate Simulation (NCCS) at Goddard Space Flight Center and from the Department of Earth Sciences at The University of Hong Kong. The authors thank for their input through multiple discussions the project members and collaborators of the ICER-1824770 project, 'Volcanism, Hydrology and Social Conflict: Lessons from Hellenistic and Roman-Era Egypt and Mesopotamia'. RS and FL acknowledge additional support from European Research Council grant agreement no. 951649 (4-OCEANS project). Aspects of this research also benefitted from discussions at workshops of the Volcanic Impacts on Climate and Society (VICS) Working Group of PAGES.

Author's contributions

RS, KT and ANL identified the study period in consultation with the other authors and RS, AK, KT, ANL and JOK designed the asynchronous coupling framework. RS and AK implemented it and performed the simulations using NASA GISS ModelE and LPJ-LMfire models. IA and RR provided the essential technical support while implementing the framework. RS and RDR created the figures in close collaboration with KT, ANL. RS wrote the first draft of the manuscript and RDR, KT, ANL, FL and JOK led the writing of subsequent drafts. All authors contributed to the interpretation of results and the drafting of the text.

Competing interests

The authors declare no competing interests.

Short Summary

This study presents an experimental framework for asynchronous land-atmosphere coupling to include biogeophysical feedbacks using a dynamic vegetation model with an Earth system model that lacks a fully dynamic vegetation component. The framework is implemented for the 2.5 ka period and also illustrates the role of model performance metrics (bias, variability), while evaluating the simulated climate against the multi-proxy paleoclimate reconstructions.

References

Aleinov, I. and Schmidt, G. A.: Water isotopes in the GISS ModelE land surface scheme, Global and Planetary Change, 51, 108–120, https://doi.org/10.1016/j.gloplacha.2005.12.010, 2006.

Baker, A., Hartmann, A., Duan, W., Hankin, S., Comas-Bru, L., Cuthbert, M. O., Treble, P. C., Banner, J., Genty, D., Baldini, L. M., Bartolomé, M., Moreno, A., Pérez-Mejías, C., and Werner, M.: Global analysis reveals climatic controls on the oxygen isotope composition of cave drip water, Nat Commun, 10, 2984, https://doi.org/10.1038/s41467-019-11027-w, 2019.

Bauer, S. E., Tsigaridis, K., Faluvegi, G., Kelley, M., Lo, K. K., Miller, R. L., Nazarenko, L., Schmidt, G. A., and Wu, J.: Historical (1850–2014) Aerosol Evolution and Role on Climate Forcing Using the GISS ModelE2.1 Contribution to CMIP6, Journal of Advances in Modeling Earth Systems, 12, e2019MS001978, https://doi.org/10.1029/2019MS001978, 2020.

Berger, A., Loutre, M. F., and Mélice, J. L.: Equatorial insolation: from precession harmonics to eccentricity frequencies, Climate of the Past, 2, 131–136, https://doi.org/10.5194/cp-2-131-2006, 2006.

869 Betts, R. A.: Offset of the potential carbon sink from boreal forestation by decreases in surface
870 albedo, Nature, 408, 187–190, https://doi.org/10.1038/35041545, 2000.

871 Bonan, G. B.: Forests and Climate Change: Forcings, Feedbacks, and the Climate Benefits of
872 Forests, Science, 320, 1444–1449, https://doi.org/10.1126/science.1155121, 2008.

873 Bonan, G. B., Pollard, D., and Thompson, S. L.: Effects of boreal forest vegetation on global
874 climate, Nature, 359, 716–718, https://doi.org/10.1038/359716a0, 1992.

875 Braconnot, P., Harrison, S. P., Kageyama, M., Bartlein, P. J., Masson-Delmotte, V., Abe-Ouchi,
876 A., Otto-Bliesner, B., and Zhao, Y.: Evaluation of climate models using palaeoclimatic data,
877 Nature Clim Change, 2, 417–424, https://doi.org/10.1038/nclimate1456, 2012.

878 Chandan, D. and Peltier, W. R.: African Humid Period Precipitation Sustained by Robust
879 Vegetation, Soil, and Lake Feedbacks, Geophysical Research Letters, 47, e2020GL088728,
880 https://doi.org/10.1029/2020GL088728, 2020.

881 Charney, J., Quirk, W. J., Chow, S., and Kornfield, J.: A Comparative Study of the Effects of
882 Albedo Change on Drought in Semi–Arid Regions, Journal of the Atmospheric Sciences, 34,
883 1366–1385, https://doi.org/10.1175/1520-0469(1977)034<1366:ACSOTE>2.0.CO;2, 1977.

884 Charney, J. G.: Dynamics of deserts and drought in the Sahel, Quarterly Journal of the Royal
885 Meteorological Society, 101, 193–202, https://doi.org/10.1002/qj.49710142802, 1975.

886 Claussen, M.: Modeling bio-geophysical feedback in the African and Indian monsoon region,
887 Climate Dynamics, 13, 247–257, https://doi.org/10.1007/s003820050164, 1997.

888 Claussen*, M.: Late Quaternary vegetation-climate feedbacks, Climate of the Past, 5, 203–216,
889 https://doi.org/10.5194/cp-5-203-2009, 2009.

890 Collins, J. A., Prange, M., Caley, T., Gimeno, L., Beckmann, B., Mulitza, S., Skonieczny, C.,
891 Roche, D., and Schefuß, E.: Rapid termination of the African Humid Period triggered by
892 northern high-latitude cooling, Nat Commun, 8, 1372, https://doi.org/10.1038/s41467-017-
893 01454-y, 2017.

894 Comas-Bru, L., Atsawawaranunt, K., Harrison, S., and members, S. working group: SISAL
895 (Speleothem Isotopes Synthesis and AnaLysis Working Group) database version 2.0,
896 https://doi.org/10.17864/1947.256, 2020.

897 Cox, P. M., Betts, R. A., Jones, C. D., Spall, S. A., and Totterdell, I. J.: Acceleration of global
898 warming due to carbon-cycle feedbacks in a coupled climate model, Nature, 408, 184–187,
899 https://doi.org/10.1038/35041539, 2000.

900 Dallmeyer, A., Claussen, M., Lorenz, S. J., Sigl, M., Toohey, M., and Herzschuh, U.: Holocene
901 vegetation transitions and their climatic drivers in MPI-ESM1.2, Climate of the Past, 17, 2481–
902 2513, https://doi.org/10.5194/cp-17-2481-2021, 2021.

Doherty, R., Kutzbach, J., Foley, J., and Pollard, D.: Fully coupled climate/dynamical vegetation model simulations over Northern Africa during the mid-Holocene, Climate Dynamics, 16, 561–573, https://doi.org/10.1007/s003820000065, 2000.

Doughty, C. E., Loarie, S. R., and Field, C. B.: Theoretical Impact of Changing Albedo on Precipitation at the Southernmost Boundary of the ITCZ in South America, Earth Interactions, 16, 1–14, https://doi.org/10.1175/2012EI422.1, 2012.

Doughty, C. E., Santos-Andrade, P. E., Shenkin, A., Goldsmith, G. R., Bentley, L. P., Blonder, B., Díaz, S., Salinas, N., Enquist, B. J., Martin, R. E., Asner, G. P., and Malhi, Y.: Tropical forest leaves may darken in response to climate change, Nat Ecol Evol, 2, 1918–1924, https://doi.org/10.1038/s41559-018-0716-y, 2018.

Eyring, V., Bony, S., Meehl, G. A., Senior, C. A., Stevens, B., Stouffer, R. J., and Taylor, K. E.: Overview of the Coupled Model Intercomparison Project Phase 6 (CMIP6) experimental design and organization, Geoscientific Model Development, 9, 1937–1958, https://doi.org/10.5194/gmd-9-1937-2016, 2016.

Fekete, B. M., Vörösmarty, C. J., and Lammers, R. B.: Scaling gridded river networks for macroscale hydrology: Development, analysis, and control of error, Water Resources Research, 37, 1955–1967, https://doi.org/10.1029/2001WR900024, 2001.

Gao, F., Morisette, J. T., Wolfe, R. E., Ederer, G., Pedelty, J., Masuoka, E., Myneni, R., Tan, B., and Nightingale, J.: An Algorithm to Produce Temporally and Spatially Continuous MODIS-LAI Time Series, IEEE Geoscience and Remote Sensing Letters, 5, 60–64, https://doi.org/10.1109/LGRS.2007.907971, 2008.

Hamilton, D. S., Hantson, S., Scott, C. E., Kaplan, J. O., Pringle, K. J., Nieradzik, L. P., Rap, A., Folberth, G. A., Spracklen, D. V., and Carslaw, K. S.: Reassessment of pre-industrial fire emissions strongly affects anthropogenic aerosol forcing, Nat Commun, 9, 3182, https://doi.org/10.1038/s41467-018-05592-9, 2018.

Harris, I., Osborn, T. J., Jones, P., and Lister, D.: Version 4 of the CRU TS monthly high-resolution gridded multivariate climate dataset, Sci Data, 7, 109, https://doi.org/10.1038/s41597-020-0453-3, 2020.

Harrison, S. P., Bartlein, P. J., Izumi, K., Li, G., Annan, J., Hargreaves, J., Braconnot, P., and Kageyama, M.: Evaluation of CMIP5 palaeo-simulations to improve climate projections, Nature Clim Change, 5, 735–743, https://doi.org/10.1038/nclimate2649, 2015.

Hartmann, A. and Baker, A.: Modelling karst vadose zone hydrology and its relevance for paleoclimate reconstruction, Earth-Science Reviews, 172, 178–192, https://doi.org/10.1016/j.earscirev.2017.08.001, 2017.

Henderson, K., Laube, A., Gäggeler, H. W., Olivier, S., Papina, T., and Schwikowski, M.: Temporal variations of accumulation and temperature during the past two centuries from Belukha ice core, Siberian Altai, Journal of Geophysical Research: Atmospheres, 111, https://doi.org/10.1029/2005JD005819, 2006.

941 Hoesly, R. M., Smith, S. J., Feng, L., Klimont, Z., Janssens-Maenhout, G., Pitkanen, T., Seibert,
942 J. J., Vu, L., Andres, R. J., Bolt, R. M., Bond, T. C., Dawidowski, L., Kholod, N., Kurokawa, J.,
943 Li, M., Liu, L., Lu, Z., Moura, M. C. P., O'Rourke, P. R., and Zhang, Q.: Historical (1750–2014)
944 anthropogenic emissions of reactive gases and aerosols from the Community Emissions Data
945 System (CEDS), Geoscientific Model Development, 11, 369–408, https://doi.org/10.5194/gmd-
946 11-369-2018, 2018.

947 Ito, G., Romanou, A., Kiang, N. Y., Faluvegi, G., Aleinov, I., Ruedy, R., Russell, G., Lerner, P.,
948 Kelley, M., and Lo, K.: Global Carbon Cycle and Climate Feedbacks in the NASA GISS
949 ModelE2.1, Journal of Advances in Modeling Earth Systems, 12, e2019MS002030,
950 https://doi.org/10.1029/2019MS002030, 2020.

951 Jahn, B., Schneider, R. R., Müller, P.-J., Donner, B., and Röhl, U.: Response of tropical African
952 and East Atlantic climates to orbital forcing over the last 1.7 Ma, Geological Society, London,
953 Special Publications, 247, 65–84, https://doi.org/10.1144/GSL.SP.2005.247.01.04, 2005.

954 Kageyama, M., Braconnot, P., Harrison, S. P., Haywood, A. M., Jungclaus, J. H., Otto-Bliesner,
955 B. L., Peterschmitt, J.-Y., Abe-Ouchi, A., Albani, S., Bartlein, P. J., Brierley, C., Crucifix, M.,
956 Dolan, A., Fernandez-Donado, L., Fischer, H., Hopcroft, P. O., Ivanovic, R. F., Lambert, F.,
957 Lunt, D. J., Mahowald, N. M., Peltier, W. R., Phipps, S. J., Roche, D. M., Schmidt, G. A.,
958 Tarasov, L., Valdes, P. J., Zhang, Q., and Zhou, T.: The PMIP4 contribution to CMIP6 – Part 1:
959 Overview and over-arching analysis plan, Geoscientific Model Development, 11, 1033–1057,
960 https://doi.org/10.5194/gmd-11-1033-2018, 2018.

961 Kaplan, J. O., Krumhardt, K. M., and Zimmermann, N. E.: The effects of land use and climate
962 change on the carbon cycle of Europe over the past 500 years, Global Change Biology, 18, 902–
963 914, https://doi.org/10.1111/j.1365-2486.2011.02580.x, 2012.

964 Kaplan, J. O., Koch, A., and Vitali, R.: ARVE-Research/LPJ-LMfire: LPJ-LMfire (tropical
965 forest restoration), , https://doi.org/10.5281/zenodo.5831747, 2022.

966 Kattge, J., Díaz, S., Lavorel, S., Prentice, I. C., Leadley, P., Bönisch, G., Garnier, E., Westoby,
967 M., Reich, P. B., Wright, I. J., Cornelissen, J. H. C., Violle, C., Harrison, S. P., Van BODEGOM,
968 P. M., Reichstein, M., Enquist, B. J., Soudzilovskaia, N. A., Ackerly, D. D., Anand, M., Atkin,
969 O., Bahn, M., Baker, T. R., Baldocchi, D., Bekker, R., Blanco, C. C., Blonder, B., Bond, W. J.,
970 Bradstock, R., Bunker, D. E., Casanoves, F., Cavender-Bares, J., Chambers, J. Q., Chapin Iii, F.
971 S., Chave, J., Coomes, D., Cornwell, W. K., Craine, J. M., Dobrin, B. H., Duarte, L., Durka, W.,
972 Elser, J., Esser, G., Estiarte, M., Fagan, W. F., Fang, J., Fernández-Méndez, F., Fidelis, A.,
973 Finegan, B., Flores, O., Ford, H., Frank, D., Freschet, G. T., Fyllas, N. M., Gallagher, R. V.,
974 Green, W. A., Gutierrez, A. G., Hickler, T., Higgins, S. I., Hodgson, J. G., Jalili, A., Jansen, S.,
975 Joly, C. A., Kerkhoff, A. J., Kirkup, D., Kitajima, K., Kleyer, M., Klotz, S., Knops, J. M. H.,
976 Kramer, K., Kühn, I., Kurokawa, H., Laughlin, D., Lee, T. D., Leishman, M., Lens, F., Lenz, T.,
977 Lewis, S. L., Lloyd, J., Llusià, J., Louault, F., Ma, S., Mahecha, M. D., Manning, P., Massad, T.,
978 Medlyn, B. E., Messier, J., Moles, A. T., Müller, S. C., Nadrowski, K., Naeem, S., Niinemets,
979 Ü., Nöllert, S., Nüske, A., Ogaya, R., Oleksyn, J., Onipchenko, V. G., Onoda, Y., Ordoñez, J.,
980 Overbeck, G., et al.: TRY – a global database of plant traits, Global Change Biology, 17, 2905–
981 2935, https://doi.org/10.1111/j.1365-2486.2011.02451.x, 2011.

Kaufman, D., McKay, N., Routson, C., Erb, M., Dätwyler, C., Sommer, P. S., Heiri, O., and Davis, B.: Holocene global mean surface temperature, a multi-method reconstruction approach, Sci Data, 7, 201, https://doi.org/10.1038/s41597-020-0530-7, 2020.

Kelley, M., Schmidt, G. A., Nazarenko, L. S., Bauer, S. E., Ruedy, R., Russell, G. L., Ackerman, A. S., Aleinov, I., Bauer, M., Bleck, R., Canuto, V., Cesana, G., Cheng, Y., Clune, T. L., Cook, B. I., Cruz, C. A., Del Genio, A. D., Elsaesser, G. S., Faluvegi, G., Kiang, N. Y., Kim, D., Lacis, A. A., Leboissetier, A., LeGrande, A. N., Lo, K. K., Marshall, J., Matthews, E. E., McDermid, S., Mezuman, K., Miller, R. L., Murray, L. T., Oinas, V., Orbe, C., García-Pando, C. P., Perlwitz, J. P., Puma, M. J., Rind, D., Romanou, A., Shindell, D. T., Sun, S., Tausnev, N., Tsigaridis, K., Tselioudis, G., Weng, E., Wu, J., and Yao, M.-S.: GISS-E2.1: Configurations and Climatology, Journal of Advances in Modeling Earth Systems, 12, e2019MS002025, https://doi.org/10.1029/2019MS002025, 2020.

Kim, Y., Moorcroft, P. R., Aleinov, I., Puma, M. J., and Kiang, N. Y.: Variability of phenology and fluxes of water and carbon with observed and simulated soil moisture in the Ent Terrestrial Biosphere Model (Ent TBM version 1.0.1.0.0), Geoscientific Model Development, 8, 3837–3865, https://doi.org/10.5194/gmd-8-3837-2015, 2015.

Kjellstroem, E., Strandberg, G., Brandefelt, J., Naeslund, J.-O., Smith, B., and Wohlfarth, B.: Climate conditions in Sweden in a 100,000-year time perspective, 2009.

Köhler, P., Nehrbass-Ahles, C., Schmitt, J., Stocker, T. F., and Fischer, H.: A 156 kyr smoothed history of the atmospheric greenhouse gases CO_2, CH_4, and N_2O and their radiative forcing, Earth System Science Data, 9, 363–387, https://doi.org/10.5194/essd-9-363-2017, 2017.

Kubatzki, C. and Claussen, M.: Simulation of the global bio-geophysical interactions during the Last Glacial Maximum, Climate Dynamics, 14, 461–471, https://doi.org/10.1007/s003820050234, 1998.

Kurita, N., Yoshida, N., Inoue, G., and Chayanova, E. A.: Modern isotope climatology of Russia: A first assessment, Journal of Geophysical Research: Atmospheres, 109, https://doi.org/10.1029/2003JD003404, 2004.

Lachniet, M. S.: Climatic and environmental controls on speleothem oxygen-isotope values, Quaternary Science Reviews, 28, 412–432, https://doi.org/10.1016/j.quascirev.2008.10.021, 2009.

Lamb, P. J.: Persistence of Subsaharan drought, Nature, 299, 46–48, https://doi.org/10.1038/299046a0, 1982.

LeGrande, A. N. and Schmidt, G. A.: Global gridded data set of the oxygen isotopic composition in seawater, Geophysical Research Letters, 33, https://doi.org/10.1029/2006GL026011, 2006.

Li, C.-F., Chytrý, M., Zelený, D., Chen, M.-Y., Chen, T.-Y., Chiou, C.-R., Hsia, Y.-J., Liu, H.-Y., Yang, S.-Z., Yeh, C.-L., Wang, J.-C., Yu, C.-F., Lai, Y.-J., Chao, W.-C., and Hsieh, C.-F.: Classification of Taiwan forest vegetation, Applied Vegetation Science, 16, 698–719, https://doi.org/10.1111/avsc.12025, 2013.

Loulergue, L., Schilt, A., Spahni, R., Masson-Delmotte, V., Blunier, T., Lemieux, B., Barnola, J.-M., Raynaud, D., Stocker, T. F., and Chappellaz, J.: Orbital and millennial-scale features of atmospheric CH4 over the past 800,000 years, Nature, 453, 383–386, https://doi.org/10.1038/nature06950, 2008.

Ludlow, F. and Manning, J. G.: Volcanic Eruptions, Veiled Suns, and Nile Failure in Egyptian History: Integrating Hydroclimate into Understandings of Historical Change, in: Climate Change and Ancient Societies in Europe and the Near East: Diversity in Collapse and Resilience, edited by: Erdkamp, P., Manning, J. G., and Verboven, K., Springer International Publishing, Cham, 301–320, https://doi.org/10.1007/978-3-030-81103-7_10, 2021.

Magi, B. I.: Global Lightning Parameterization from CMIP5 Climate Model Output, Journal of Atmospheric and Oceanic Technology, 32, 434–452, https://doi.org/10.1175/JTECH-D-13-00261.1, 2015.

Manning, J. G., Ludlow, F., Stine, A. R., Boos, W. R., Sigl, M., and Marlon, J. R.: Volcanic suppression of Nile summer flooding triggers revolt and constrains interstate conflict in ancient Egypt, Nat Commun, 8, 900, https://doi.org/10.1038/s41467-017-00957-y, 2017.

Mikhail, A.: Ottoman Iceland: A Climate History, Environmental History, 20, 262–284, https://doi.org/10.1093/envhis/emv006, 2015.

Myneni, R. B., Hoffman, S., Knyazikhin, Y., Privette, J. L., Glassy, J., Tian, Y., Wang, Y., Song, X., Zhang, Y., Smith, G. R., Lotsch, A., Friedl, M., Morisette, J. T., Votava, P., Nemani, R. R., and Running, S. W.: Global products of vegetation leaf area and fraction absorbed PAR from year one of MODIS data, Remote Sensing of Environment, 83, 214–231, https://doi.org/10.1016/S0034-4257(02)00074-3, 2002.

de Noblet, N., Braconnot, P., Joussaume, S., and Masson, V.: Sensitivity of simulated Asian and African summer monsoons to orbitally induced variations in insolation 126, 115 and 6 kBP, Climate Dynamics, 12, 589–603, https://doi.org/10.1007/BF00216268, 1996.

Otto-Bliesner, B. L., Braconnot, P., Harrison, S. P., Lunt, D. J., Abe-Ouchi, A., Albani, S., Bartlein, P. J., Capron, E., Carlson, A. E., Dutton, A., Fischer, H., Goelzer, H., Govin, A., Haywood, A., Joos, F., LeGrande, A. N., Lipscomb, W. H., Lohmann, G., Mahowald, N., Nehrbass-Ahles, C., Pausata, F. S. R., Peterschmitt, J.-Y., Phipps, S. J., Renssen, H., and Zhang, Q.: The PMIP4 contribution to CMIP6 – Part 2: Two interglacials, scientific objective and experimental design for Holocene and Last Interglacial simulations, Geoscientific Model Development, 10, 3979–4003, https://doi.org/10.5194/gmd-10-3979-2017, 2017.

Pang, G., Chen, D., Wang, X., and Lai, H.-W.: Spatiotemporal variations of land surface albedo and associated influencing factors on the Tibetan Plateau, Science of The Total Environment, 804, 150100, https://doi.org/10.1016/j.scitotenv.2021.150100, 2022.

Pausata, F. S. R., Messori, G., and Zhang, Q.: Impacts of dust reduction on the northward expansion of the African monsoon during the Green Sahara period, Earth and Planetary Science Letters, 434, 298–307, https://doi.org/10.1016/j.epsl.2015.11.049, 2016.

Petit-Maire, N. and Guo, Z. T.: Mid-Holocene climatic change and man in the present-day Sahara desert, in: Quaternary Deserts and Climatic Change, CRC Press, 1998.

Pfeiffer, M., Spessa, A., and Kaplan, J. O.: A model for global biomass burning in preindustrial time: LPJ-LMfire (v1.0), Geoscientific Model Development, 6, 643–685, https://doi.org/10.5194/gmd-6-643-2013, 2013.

Rachmayani, R., Prange, M., and Schulz, M.: North African vegetation–precipitation feedback in early and mid-Holocene climate simulations with CCSM3-DGVM, Climate of the Past, 11, 175–185, https://doi.org/10.5194/cp-11-175-2015, 2015.

Reale, O. and Dirmeyer, P.: Modeling the effects of vegetation on Mediterranean climate during the Roman Classical Period: Part I: Climate history and model sensitivity, Global and Planetary Change, 25, 163–184, https://doi.org/10.1016/S0921-8181(00)00002-3, 2000.

Schmidt, G. A.: Oxygen-18 variations in a global ocean model, Geophysical Research Letters, 25, 1201–1204, https://doi.org/10.1029/98GL50866, 1998.

Schneider, R., Schmitt, J., Köhler, P., Joos, F., and Fischer, H.: A reconstruction of atmospheric carbon dioxide and its stable carbon isotopic composition from the penultimate glacial maximum to the last glacial inception, Climate of the Past, 9, 2507–2523, https://doi.org/10.5194/cp-9-2507-2013, 2013.

Sha, L., Ait Brahim, Y., Wassenburg, J. A., Yin, J., Peros, M., Cruz, F. W., Cai, Y., Li, H., Du, W., Zhang, H., Edwards, R. L., and Cheng, H.: How Far North Did the African Monsoon Fringe Expand During the African Humid Period? Insights From Southwest Moroccan Speleothems, Geophysical Research Letters, 46, 14093–14102, https://doi.org/10.1029/2019GL084879, 2019.

Shanahan, T. M., McKay, N. P., Hughen, K. A., Overpeck, J. T., Otto-Bliesner, B., Heil, C. W., King, J., Scholz, C. A., and Peck, J.: The time-transgressive termination of the African Humid Period, Nature Geosci, 8, 140–144, https://doi.org/10.1038/ngeo2329, 2015.

Siegenthaler, U., Stocker, T. F., Monnin, E., Lüthi, D., Schwander, J., Stauffer, B., Raynaud, D., Barnola, J.-M., Fischer, H., Masson-Delmotte, V., and Jouzel, J.: Stable Carbon Cycle□Climate Relationship During the Late Pleistocene, Science, 310, 1313–1317, https://doi.org/10.1126/science.1120130, 2005.

Simard, M., Pinto, N., Fisher, J. B., and Baccini, A.: Mapping forest canopy height globally with spaceborne lidar, Journal of Geophysical Research: Biogeosciences, 116, https://doi.org/10.1029/2011JG001708, 2011.

Singh, R., Tsigaridis, K., LeGrande, A. N., Ludlow, F., and Manning, J. G.: Investigating hydroclimatic impacts of the 168–158 BCE volcanic quartet and their relevance to the Nile River basin and Egyptian history, Climate of the Past, 19, 249–275, https://doi.org/10.5194/cp-19-249-2023, 2023.

Singh, R., Koch, A., LeGrande, A. N., Tsigaridis, K., Ramos, R. D., Ludlow, F., Aleinov, I., Ruedy, R., and Kaplan, J. O.: Modelling framework for asynchronous land-atmosphere coupling

using NASA GISS ModelE and LPJ-LMfire: Design, Application and Evaluation for the 2.5ka period, https://doi.org/10.5281/zenodo.13626434, 2024.

Sitch, S., Smith, B., Prentice, I. C., Arneth, A., Bondeau, A., Cramer, W., Kaplan, J. O., Levis, S., Lucht, W., Sykes, M. T., Thonicke, K., and Venevsky, S.: Evaluation of ecosystem dynamics, plant geography and terrestrial carbon cycling in the LPJ dynamic global vegetation model, Global Change Biology, 9, 161–185, https://doi.org/10.1046/j.1365-2486.2003.00569.x, 2003.

Stocker, T. F., Qin, D., Plattner, G.-K., Tignor, M. M. B., Allen, S. K., Boschung, J., Nauels, A., Xia, Y., Bex, V., Midgley, P. M., Alexander, L. V., Allen, S. K., Bindoff, N. L., Breon, F.-M., Church, J. A., Cubasch, U., Emori, S., Forster, P., Friedlingstein, P., Gillett, N., Gregory, J. M., Hartmann, D. L., Jansen, E., Kirtman, B., Knutti, R., Kumar Kanikicharla, K., Lemke, P., Marotzke, J., Masson-Delmotte, V., Meehl, G. A., Mokhov, I. I., Piao, S., Plattner, G.-K., Dahe, Q., Ramaswamy, V., Randall, D., Rhein, M., Rojas, M., Sabine, C., Shindell, D., Stocker, T. F., Talley, L. D., Vaughan, D. G., Xie, S.-P., Allen, M. R., Boucher, O., Chambers, D., Hesselbjerg Christensen, J., Ciais, P., Clark, P. U., Collins, M., Comiso, J. C., Vasconcellos de Menezes, V., Feely, R. A., Fichefet, T., Fiore, A. M., Flato, G., Fuglestvedt, J., Hegerl, G., Hezel, P. J., Johnson, G. C., Kaser, G., Kattsov, V., Kennedy, J., Klein Tank, A. M. G., Le Quere, C., Myhre, G., Osborn, T., Payne, A. J., Perlwitz, J., Power, S., Prather, M., Rintoul, S. R., Rogelj, J., Rusticucci, M., Schulz, M., Sedlacek, J., Stott, P. A., Sutton, R., Thorne, P. W., and Wuebbles, D.: Climate Change 2013. The Physical Science Basis. Working Group I Contribution to the Fifth Assessment Report of the Intergovernmental Panel on Climate Change - Abstract for decision-makers; Changements climatiques 2013. Les elements scientifiques. Contribution du groupe de travail I au cinquieme rapport d'evaluation du groupe d'experts intergouvernemental sur l'evolution du CLIMAT - Resume a l'intention des decideurs, 2013.

Strandberg, G., Brandefelt, J., Kjellstro¨M, E., and Smith, B.: High-resolution regional simulation of last glacial maximum climate in Europe, Tellus A: Dynamic Meteorology and Oceanography, 63, 107–125, https://doi.org/10.1111/j.1600-0870.2010.00485.x, 2011.

Strandberg, G., Kjellström, E., Poska, A., Wagner, S., Gaillard, M.-J., Trondman, A.-K., Mauri, A., Davis, B. a. S., Kaplan, J. O., Birks, H. J. B., Bjune, A. E., Fyfe, R., Giesecke, T., Kalnina, L., Kangur, M., van der Knaap, W. O., Kokfelt, U., Kuneš, P., Lata\l owa, M., Marquer, L., Mazier, F., Nielsen, A. B., Smith, B., Seppä, H., and Sugita, S.: Regional climate model simulations for Europe at 6 and 0.2 k BP: sensitivity to changes in anthropogenic deforestation, Climate of the Past, 10, 661–680, https://doi.org/10.5194/cp-10-661-2014, 2014a.

Strandberg, G., Kjellström, E., Poska, A., Wagner, S., Gaillard, M.-J., Trondman, A.-K., Mauri, A., Davis, B. a. S., Kaplan, J. O., Birks, H. J. B., Bjune, A. E., Fyfe, R., Giesecke, T., Kalnina, L., Kangur, M., van der Knaap, W. O., Kokfelt, U., Kuneš, P., Lata\l owa, M., Marquer, L., Mazier, F., Nielsen, A. B., Smith, B., Seppä, H., and Sugita, S.: Regional climate model simulations for Europe at 6 and 0.2 k BP: sensitivity to changes in anthropogenic deforestation, Climate of the Past, 10, 661–680, https://doi.org/10.5194/cp-10-661-2014, 2014b.

Swann, A. L., Fung, I. Y., Levis, S., Bonan, G. B., and Doney, S. C.: Changes in Arctic vegetation amplify high-latitude warming through the greenhouse effect, Proceedings of the

National Academy of Sciences, 107, 1295–1300, https://doi.org/10.1073/pnas.0913846107, 2010.

Texier, D., De Noblet, N., Harrison, S. P., Haxeltine, A., Jolly, D., Joussaume, S., Laarif, F., Prentice, I. C., and Tarasov, P.: Quantifying the role of biosphere-atmosphere feedbacks in climate change: Coupled model simulations for 6000 years BP and comparison with palaeodata for northern Eurasia and northern Africa, Climate Dynamics, 13, 865–882, 1997.

Thomas, G. and Rowntree, P. R.: The Boreal Forests and Climate, Quarterly Journal of the Royal Meteorological Society, 118, 469–497, https://doi.org/10.1002/qj.49711850505, 1992.

Thompson, A. J., Tabor, C. R., Poulsen, C. J., and Skinner, C. B.: Water isotopic constraints on the enhancement of the mid-Holocene West African monsoon, Earth and Planetary Science Letters, 554, 116677, https://doi.org/10.1016/j.epsl.2020.116677, 2021.

Thonicke, K., Spessa, A., Prentice, I. C., Harrison, S. P., Dong, L., and Carmona-Moreno, C.: The influence of vegetation, fire spread and fire behaviour on biomass burning and trace gas emissions: results from a process-based model, Biogeosciences, 7, 1991–2011, https://doi.org/10.5194/bg-7-1991-2010, 2010.

Tian, Y., Woodcock, C. E., Wang, Y., Privette, J. L., Shabanov, N. V., Zhou, L., Zhang, Y., Buermann, W., Dong, J., Veikkanen, B., Häme, T., Andersson, K., Ozdogan, M., Knyazikhin, Y., and Myneni, R. B.: Multiscale analysis and validation of the MODIS LAI product: I. Uncertainty assessment, Remote Sensing of Environment, 83, 414–430, https://doi.org/10.1016/S0034-4257(02)00047-0, 2002a.

Tian, Y., Woodcock, C. E., Wang, Y., Privette, J. L., Shabanov, N. V., Zhou, L., Zhang, Y., Buermann, W., Dong, J., Veikkanen, B., Häme, T., Andersson, K., Ozdogan, M., Knyazikhin, Y., and Myneni, R. B.: Multiscale analysis and validation of the MODIS LAI product: II. Sampling strategy, Remote Sensing of Environment, 83, 431–441, https://doi.org/10.1016/S0034-4257(02)00058-5, 2002b.

Tierney, J. E., Pausata, F. S. R., and deMenocal, P. B.: Rainfall regimes of the Green Sahara, Science Advances, 3, e1601503, https://doi.org/10.1126/sciadv.1601503, 2017.

Tiwari, S., Ramos, R. D., Pausata, F. S. R., LeGrande, A. N., Griffiths, M. L., Beltrami, H., Wainer, I., de Vernal, A., Litchmore, D. T., Chandan, D., Peltier, W. R., and Tabor, C. R.: On the Remote Impacts of Mid-Holocene Saharan Vegetation on South American Hydroclimate: A Modeling Intercomparison, Geophysical Research Letters, 50, e2022GL101974, https://doi.org/10.1029/2022GL101974, 2023.

Velasquez, P., Kaplan, J. O., Messmer, M., Ludwig, P., and Raible, C. C.: The role of land cover in the climate of glacial Europe, Climate of the Past, 17, 1161–1180, https://doi.org/10.5194/cp-17-1161-2021, 2021.

Yang, W., Tan, B., Huang, D., Rautiainen, M., Shabanov, N. V., Wang, Y., Privette, J. L., Huemmrich, K. F., Fensholt, R., Sandholt, I., Weiss, M., Ahl, D. E., Gower, S. T., Nemani, R. R., Knyazikhin, Y., and Myneni, R. B.: MODIS leaf area index products: from validation to

algorithm improvement, IEEE Transactions on Geoscience and Remote Sensing, 44, 1885–1898, https://doi.org/10.1109/TGRS.2006.871215, 2006.

Zeng, Z., Wang, D., Yang, L., Wu, J., Ziegler, A. D., Liu, M., Ciais, P., Searchinger, T. D., Yang, Z.-L., Chen, D., Chen, A., Li, L. Z. X., Piao, S., Taylor, D., Cai, X., Pan, M., Peng, L., Lin, P., Gower, D., Feng, Y., Zheng, C., Guan, K., Lian, X., Wang, T., Wang, L., Jeong, S.-J., Wei, Z., Sheffield, J., Caylor, K., and Wood, E. F.: Deforestation-induced warming over tropical mountain regions regulated by elevation, Nat. Geosci., 14, 23–29, https://doi.org/10.1038/s41561-020-00666-0, 2021.